

Estimation of the Hubble parameter from unedited compact object merger catalogues

Reiko Harada,^{1,2,*} Heather Fong,³ and Kipp Cannon^{1,†}

¹*Research Center for the Early Universe (RESCEU),
Graduate School of Science, The University of Tokyo, Tokyo 113-0033, Japan*

²*Department of Physics, Graduate School of Science,
The University of Tokyo, Tokyo 113-0033, Japan*

³*University of British Columbia, Vancouver Campus,
2329 West Mall, Vancouver, British Columbia V6T 1Z4, Canada*

In recent years, constraints on the Hubble parameter using multiple dark sirens have been made, relying on a galaxy catalogue, correlations between the mass and redshift distributions, or both. Those studies have typically used only significant gravitational wave candidates. In this work, we present a framework for cosmological inference that bypasses per-candidate parameter estimation, uses only detection-level information. This allows the population inference from a candidate list produced directly by a search pipeline, without additional selection cuts. Our method is particularly suited to extracting information from marginal candidates, which are essential for probing the distant universe.

I. INTRODUCTION

The idea of using gravitational wave (GW) to measure the cosmological parameters was first proposed by Schutz (1986), as the “standard siren” idea [1]. This vision became reality decades later, with the LIGO/Virgo detection of the binary neutron star (BNS) merger GW170817, where the electromagnetic (EM) counterpart enabled host-galaxy identification and thus a redshift, which combined with the GW-inferred luminosity distance to yield a direct H_0 measurement [2]. GW170817 remains the only bright siren (with confirmed EM counterpart) to date; most GW detections are binary black hole (BBH) mergers that lack observable EM signatures [3–7]. Consequently, recent research has turned to “dark siren” methods: statistically inferring cosmological parameters from GW candidates without EM counterparts [8]. These methods typically utilize external information such as galaxy catalogues [9–13] or any other assumed source redshift distributions [12–16] in a hierarchical Bayesian framework. In essence, cosmological parameters including H_0 are treated as a population parameters governing the spatial distribution of compact binary coalescence (CBC) candidates, and constraints on its value are obtained by comparing the observed distribution of luminosity distances (or equivalently, signal-to-noise ratio (SNR)) with the assumed redshift distribution. A key feature of these analyses is that observed (detector-frame) masses are redshifted, entangling the mass distribution with cosmological parameters [17, 18]. This coupling both creates opportunities (e.g., “spectral sirens”) [19] and highlights the need to jointly infer cosmology and population parameters to avoid bias [12, 13]. This is how cosmology has become an integral part of GW population analysis—recent works incorporate H_0 into pop-

ulation models and estimate it jointly with astrophysical parameters.

Despite the progress, most GW cosmology (population) studies so far have been limited to the most significant candidates. For example, the GWTC-3 catalogue (through the end of LIGO/Virgo’s third observing run) contained 90 CBC candidates, yet cosmological inferences were performed using 47 significant candidates, with a network matched filter SNR > 11 and an inverse false-alarm rate (IFAR) higher than 4 years [12]. Also, the latest LIGO–Virgo–KAGRA (LVK) analysis (GWTC-4.0, covering up to the first part of the fourth observing run) used 142 out of 218 total candidates to constrain H_0 and population properties, and the candidates are selected with the lowest false-alarm rate (FAR) among all search pipelines, ensuring all candidates have IFAR higher than 4 years [13].

We consider that there are two main reasons for this reliance on a high significance threshold. First, conventional GW hierarchical inference requires a posterior samples in the CBC parameter space for each candidate, obtained via full parameter estimation (PE) [11, 15, 20–24]. This is a computationally expensive process and is thus usually conducted only for candidates with a high significance. While recent advances (e.g. neural network surrogate models [25–29]) have enabled low-latency generation of PE posteriors, applying PE to every low-significance candidate is not yet standard. Second, if one lowers the threshold to include marginal candidates, one inevitably introduces false alarms (noise-originating candidates) into the catalogue. Analyzing a mixture of real signals and noise-originating candidates demands a multi-population modeling approach: one must simultaneously account for the astrophysical population of CBCs and the background “population” of noise candidates [20, 21, 30–34]. However, implementing a rigorous joint inference with an unknown noise population is challenging—the distribution of noise-originating candidates in the CBC parameter space is not well understood, and any mis-specification can bias the inferences.

* harada.reiko@resceu.s.u-tokyo.ac.jp

† kipp@resceu.s.u-tokyo.ac.jp

Although some previous studies have proposed to directly incorporate the background population model of the search pipelines through the use of $p(\text{astro})$ [31, 32], many population analyses to date have tended to avoid these complications by simply discarding lower-significance candidates.

In this paper, we propose a new framework for GW population inference that is capable of incorporating candidates across a wide range of statistical significance, working directly with detection-level information. Our approach operates on a CBC catalogue produced by a GW search pipeline, GstLAL [35], and requires, for each CBC candidate, only its detection statistic, together with the signal and noise models adopted in the search to compute significance (e.g. the models underlying FAR [36] and $p(\text{astro})$ [20, 30, 37–42] calculations). Conventional hierarchical analyses generally rely on large-scale injection campaigns to estimate the detection efficiency and correct for selection biases [21, 43, 44]. In contrast, since our dataset consists of detection statistics that already reflect the search threshold, our framework inherently incorporates the selection imposed by the search, without requiring explicit injection-based sensitivity estimates.

We develop this framework and demonstrate it as a proof of concept for cosmology. In particular, we focus on estimating the Hubble constant from a mock catalogue of CBCs, showing how our approach can recover H_0 from the observational dataset. We emphasize that the primary goal of this work is to introduce and validate the methodology, rather than to present scientific results of cosmological measurement. Although our demonstration focuses on H_0 , it can be extended to jointly infer H_0 alongside other population parameters (e.g. the merger rate evolution or mass distribution parameters). It should be noted, however, that GstLAL's signal and noise models, as the probability density functions (PDFs) of the detection statistic, are not known in analytic form; they are constructed numerically through importance sampling [45]. Consequently, if the number of samples is insufficient or the resulting PDFs are not well converged, the residual fluctuations in the detection-statistic PDFs may exhibit dependence on the population parameters, which in turn can bias the population inference. This issue, revealed through our mock data analyses (MDAs), represents one of the key limitations of our current framework and points toward important directions for future improvement.

This paper is organized as follows. In Sec. II, we describe our framework for population inference, only using detection level information. Sec. III describes a mock data analysis that serves as a proof-of-concept demonstration, including both the setup and the results. Sec. IV summarizes our conclusions.

II. FRAMEWORK

A. Basics

The main goal here is to calculate a posterior distribution of the population parameters $p(\lambda|D, \Delta)$, where D is our observational dataset, Δ denotes our detection criteria and observational limitation made by instrument's sensitivity and search algorithm. Here, we define λ as the set of all parameters that determine the shape of the CBC population distribution, including the parameter describing the mass distributions of CBCs, λ_m , and the cosmological parameters, λ_c . Heinzel et al. (2023) introduced a framework that explicitly incorporates the glitch population parameters [33]. In contrast, we do not aim to infer the terrestrial noise population jointly with CBC population; instead, we treat the GstLAL noise model as a fixed, pre-characterized representation of the background population. To be confirmed later, introducing Δ in our posterior is essential to account for selection effects.

In our framework, the dataset is interpreted not as raw strain data around each GW candidate, but as the set of detection statistics assigned by a search pipeline to each GW candidate. Then, the dataset, D , is a CBC catalogue of total size N_{tot} , each of whose entries provides a detection statistic x , and our detection criteria, Δ , is that the value of detection statistic is equal or above the threshold value: $x \geq x_{\text{th}}$. This approach eliminates the need for parameter estimation of individual GW candidates and for large-scale injection campaigns to evaluate selection effects in catalogue construction. As a result, it enables population analyses of GW sources to be carried out at substantially lower computational cost, while incorporating even low-significance candidates. Furthermore, since our observational dataset generally contains a mixture of candidates originating from CBCs and those arising from terrestrial noise, following the treatment introduced by Farr et al. (2015) [30], we account for the expected numbers, \bar{R}_s and \bar{R}_n , of signal-originating and noise-originating candidates that satisfy the detection criteria Δ and occur during the observing period:

$$p(\lambda|D, \Delta) = \int_0^\infty d\bar{R}_s \int_0^\infty d\bar{R}_n p(\lambda, \bar{R}_s, \bar{R}_n|D, \Delta), \quad (1)$$

$$= \int_0^\infty d\bar{R}_{\text{tot}} \int_0^1 d\bar{\eta} p(\lambda, \bar{R}_{\text{tot}}, \bar{\eta}|D, \Delta), \quad (2)$$

$$\propto \int_0^\infty d\bar{R}_{\text{tot}} \int_0^1 d\bar{\eta} p(D|\lambda, \bar{R}_{\text{tot}}, \bar{\eta}, \Delta) \pi(\lambda, \bar{R}_{\text{tot}}, \bar{\eta}|\Delta), \quad (3)$$

where

$$\bar{R}_{\text{tot}} = \bar{R}_s + \bar{R}_n \quad (4)$$

is the expected total number of candidates, and

$$\bar{\eta} = \frac{\bar{R}_s}{\bar{R}_s + \bar{R}_n} \quad (5)$$

is the expected fraction of signal-originating candidates among the total. This quantity is basically identical to the one denoted by $\bar{\eta}$ in [33]. (3) is derived from the Bayes' theorem. The first term in (3), $p(D|\lambda, \bar{R}_{\text{tot}}, \bar{\eta}, \Delta)$, is the probability of obtaining the dataset given the hypotheses (the source population described by $\{\lambda, \bar{R}_{\text{tot}}, \bar{\eta}\}$, and the data acquisition process described by Δ), which is called the hierarchical likelihood. The second term in (3), $\pi(\lambda, \bar{R}_{\text{tot}}, \bar{\eta}|\Delta)$, is so called the prior probability and depends on our state of knowledge. Although \bar{R}_{tot} and $\bar{\eta}$ are, in principle, related to the population parameters λ and our detection criteria Δ , thorough the underlying source distribution, we treat them as free parameters in our inference. Since their dependence on λ should ultimately be refracted through the data, we do not model it explicitly here. As a practical simplification, we assume a factorized prior of the following form:

$$\pi(\lambda, \bar{R}_{\text{tot}}, \bar{\eta}|\Delta) = \pi(\lambda)\pi(\bar{R}_{\text{tot}})\pi(\bar{\eta}). \quad (6)$$

In our MDAs in Sec. III, we take $\pi(\bar{R}_{\text{tot}})$ to be log-uniform over $[0, \infty)$, as commonly done, and $\pi(\lambda)$ to be uniform within the prior range of H_0 . For the prior on $\bar{\eta}$, we consider two choices. The first is a uniform over $[0, 1]$. The second is a delta-function prior,

$$\pi(\bar{\eta}) = \delta(\bar{\eta} - \bar{\eta}'), \quad (7)$$

where $\bar{\eta}'$ denotes the point estimate of $\bar{\eta}$ obtained using the method described in Sec. II F based on $p(\text{astro})$. Here, δ represents the Dirac delta function.

While our basic framework does not rely on a specific choice of detection statistic, x , the demonstration (MDAs) presented in Sec. III uses the log-likelihood ratio (LR) ranking statistic, $\ln \mathcal{L}$, employed by GstLAL [35, 45–47], and parts of the following discussion are written with this choice in mind.

B. GstLAL likelihood-ratio ranking statistic

The GstLAL LR ranking statistic takes the form of

$$\mathcal{L} = \frac{p(\Theta|\mathcal{H}_s)}{p(\Theta|\mathcal{H}_n)} = \frac{p(\vec{O}, \vec{\rho}, \vec{\xi}^2, \vec{t}, \vec{\phi}, \vec{\theta}|\mathcal{H}_s)}{p(\vec{O}, \vec{\rho}, \vec{\xi}^2, \vec{t}, \vec{\phi}, \vec{\theta}|\mathcal{H}_n)}. \quad (8)$$

The numerator and denominator are the likelihoods of observing an n -dimensional set of parameters, $\Theta = \{\vec{O}, \vec{\rho}, \vec{\xi}^2, \vec{t}, \vec{\phi}, \vec{\theta}\}$, under the signal and noise hypothesis, respectively. This n -dimensional set includes the set of instruments involved in the observation of the candidate \vec{O} , the vectorized SNR $\vec{\rho}$, the vectorized signal-based-veto parameter $\vec{\xi}^2$, the vectorized arrival time \vec{t} , the vectorized coalescence phase $\vec{\phi}$, and the best match template parameters $\vec{\theta}$. GstLAL provides models for both the numerator and denominator, and can evaluate them for the observed parameters [45–47]. The evaluation relies not only on prior assumptions but also on empirical information, such as the time series of instrument horizon

distances and instrumental noise properties derived from observational data products. We refer to these models as the GstLAL signal model and the GstLAL noise model, respectively.

C. Hierarchical likelihood

In order to perform Bayesian parameter estimation described in (3), we need to model the hierarchical likelihood, $p(D|\lambda, \bar{R}_{\text{tot}}, \bar{\eta}, \Delta)$. We will start from the following factorization:

$$p(D|\lambda, \bar{R}_{\text{tot}}, \bar{\eta}, \Delta) = p(\{x\}, N_{\text{tot}}|\lambda, \bar{R}_{\text{tot}}, \bar{\eta}, \Delta) \quad (9)$$

$$= p(\{x\}|N_{\text{tot}}, \lambda, \bar{R}_{\text{tot}}, \bar{\eta}, \Delta)p(N_{\text{tot}}|\lambda, \bar{R}_{\text{tot}}, \bar{\eta}, \Delta). \quad (10)$$

Assuming a Poisson process, the second term in (10) depends on λ , $\bar{\eta}$ and Δ only thorough $\bar{R}_{\text{tot}} = \bar{R}_{\text{tot}}(\lambda, \bar{\eta}, \Delta)$; that is,

$$p(N_{\text{tot}}|\lambda, \bar{R}_{\text{tot}}, \bar{\eta}, \Delta) = p(N_{\text{tot}}|\bar{R}_{\text{tot}}) = \frac{\bar{R}_{\text{tot}}^{N_{\text{tot}}} e^{-\bar{R}_{\text{tot}}}}{N_{\text{tot}}!}. \quad (11)$$

Assuming further that the detector noise has an autocorrelation length much smaller than the typical interval at which candidates are identified by the pipeline, and using \mathcal{H}_s and \mathcal{H}_n to denote the signal and the noise hypothesis (see Table I), the first term in (10) can be written as:

$$\begin{aligned} p(\{x\}|N_{\text{tot}}, \lambda, \bar{R}_{\text{tot}}, \bar{\eta}, \Delta) &= \prod_{i=1}^{N_{\text{tot}}} p(x_i|\lambda, \bar{R}_{\text{tot}}, \bar{\eta}, \Delta) \quad (12) \\ &= \prod_{i=1}^{N_{\text{tot}}} [p(x_i|\mathcal{H}_s, \lambda, \bar{R}_{\text{tot}}, \bar{\eta}, \Delta)p(\mathcal{H}_s|\lambda, \bar{R}_{\text{tot}}, \bar{\eta}, \Delta) \\ &\quad + p(x_i|\mathcal{H}_n, \lambda, \bar{R}_{\text{tot}}, \bar{\eta}, \Delta)p(\mathcal{H}_n|\lambda, \bar{R}_{\text{tot}}, \bar{\eta}, \Delta)] \quad (13) \end{aligned}$$

The second term of 13, $p(\mathcal{H}_s|\lambda, \bar{R}_{\text{tot}}, \bar{\eta}, \Delta)$, corresponds to the expected fraction of astrophysical candidates in the total number of candidates:

$$p(\mathcal{H}_s|\lambda, \bar{R}_{\text{tot}}, \bar{\eta}, \Delta) = p(\mathcal{H}_s|\bar{\eta}, \Delta) = \bar{\eta}. \quad (14)$$

The last term in (13), $p(\mathcal{H}_n|\lambda, \bar{R}_{\text{tot}}, \bar{\eta}, \Delta)$, is the expected fraction of noise-originating candidates, and it is mutually exclusive with $p(\mathcal{H}_s|\bar{\eta}, \Delta)$, then

$$p(\mathcal{H}_n|\lambda, \bar{R}_{\text{tot}}, \bar{\eta}, \Delta) = p(\mathcal{H}_n|\bar{\eta}, \Delta) = 1 - \bar{\eta}. \quad (15)$$

As we define λ as the set of all parameters that determine the shape of CBC population distribution above, the first term of (13) can be simplified as, $p(x|\mathcal{H}_s, \lambda, \bar{R}_{\text{tot}}, \bar{\eta}, \Delta) = p(x|\mathcal{H}_s, \lambda, \Delta)$, and it is the single-candidate likelihood under the signal hypothesis, or the PDF of ranking statistic in the signal population. The third term in (13) is the single-candidate likelihood under the background hypothesis, and is independent of CBCs' population parameters: $p(x|\mathcal{H}_n, \lambda, \bar{R}_{\text{tot}}, \bar{\eta}, \Delta) = p(x|\mathcal{H}_n, \Delta)$. Then, we

TABLE I. Glossaries.

| | |
|--|---|
| $D = \{\{x\}, N_{\text{tot}}\}$ | Observational dataset. |
| x | Detection statistic of individual candidate. |
| N_{tot} | The total number of candidates. |
| Δ | Detection criteria and observational limitation made by instruments' sensitivity and search algorithm. |
| λ_{c} | Cosmological parameters including H_0 , Ω_{m} , <i>etc.</i> |
| H_0 | The Hubble constant. |
| Ω_{m} | The fractional matter density. |
| λ_{m} | Parameters describing the mass distribution. |
| λ | Parameters describing source population in general. |
| R_{s} | The expected number of astrophysical candidates that satisfy Δ . |
| R_{n} | The expected number of background candidates that satisfy Δ . |
| \bar{R}_{tot} | The expected total number of candidates. |
| $\bar{\eta}$ | The expected fraction of signals (astrophysical candidates) among the total number of candidates. |
| $\ln \mathcal{L}$ | Log-LR ranking statistic described in (8) which is employed as GstLAL's detection statistic. |
| $\Theta = \{\vec{O}, \vec{\rho}, \vec{\xi}^2, \vec{t}, \vec{\phi}, \vec{\theta}\}$ | Set of GstLAL's ranking statistic variables describing a candidate. |
| \vec{O} | Set of instruments involved in the observation of a candidate. |
| $\vec{\rho}$ | Vectorized SNR (Set of SNRs observed by each instrument \vec{O} : $\vec{\rho} = \{\rho_{\text{obs}, O_1}, \rho_{\text{obs}, O_2}, \dots\}$). |
| $\vec{\xi}^2$ | Vectorized signals-based-veto parameter. |
| \vec{t} | Vectorized arrival time. |
| $\vec{\phi}$ | Vectorized coalescence phase. |
| $\vec{\theta}$ | Best match template parameters. |
| \mathcal{H}_{s} | A hypothesis that the candidate has an astrophysical origin. |
| \mathcal{H}_{n} | A hypothesis that the candidate has a background origin. |
| z | Redshift. |
| θ | Set of intrinsic parameters describing a CBC source (masses, spins, etc.). |
| ρ_{obs} | SNR observed by a instrument. |
| ρ_{opt} | Expected SNR of a GW signal from a CBC which is optimally oriented and located to maximize the strain amplitude at a given instrument. |
| ρ_{comb} | Combined SNR of a instrument network. |

obtain the hierarchical likelihood of the following form:

$$p(D|\lambda, \bar{R}_{\text{tot}}, \bar{\eta}, \Delta) \propto \bar{R}_{\text{tot}}^{N_{\text{tot}}} e^{-\bar{R}_{\text{tot}}} \prod_{i=1}^{N_{\text{tot}}} [\bar{\eta} p(x_i|\mathcal{H}_{\text{s}}, \lambda, \Delta) + (1 - \bar{\eta}) p(x_i|\mathcal{H}_{\text{n}}, \Delta)]. \quad (16)$$

Substituting (6) and (16) into the marginalization expression in (3) shows that the term depending on \bar{R}_{tot} no longer depends on the population shape parameters λ :

$$p(\lambda|D, \Delta) \propto \left[\int_0^\infty d\bar{R}_{\text{tot}} \bar{R}_{\text{tot}}^{N_{\text{tot}}} e^{-\bar{R}_{\text{tot}}} \pi(\bar{R}_{\text{tot}}) \right] \int_0^1 d\bar{\eta} [\bar{\eta} p(x_i|\mathcal{H}_{\text{s}}, \lambda, \Delta) + (1 - \bar{\eta}) p(x_i|\mathcal{H}_{\text{n}}, \Delta)] \pi(\lambda) \pi(\bar{\eta}), \quad (17)$$

$$\propto \int_0^1 d\bar{\eta} [\bar{\eta} p(x_i|\mathcal{H}_{\text{s}}, \lambda, \Delta) + (1 - \bar{\eta}) p(x_i|\mathcal{H}_{\text{n}}, \Delta)] \pi(\lambda) \pi(\bar{\eta}). \quad (18)$$

As a result, our parameter estimation can be restricted to the population shape parameters λ and the signal fraction $\bar{\eta}$. It is therefore sufficient to consider the hierarchi-

cal likelihood

$$p(D|\lambda, \bar{\eta}, \Delta) \propto \prod_{i=1}^{N_{\text{tot}}} [\bar{\eta} p(x_i|\mathcal{H}_{\text{s}}, \lambda, \Delta) + (1 - \bar{\eta}) p(x_i|\mathcal{H}_{\text{n}}, \Delta)], \quad (19)$$

instead of $p(D|\lambda, \bar{R}_{\text{tot}}, \bar{\eta}, \Delta)$ in (16).

The difference between $p(x|\mathcal{H}_s, \lambda)$ and $p(x|\mathcal{H}_s, \lambda, \Delta)$ is basically just the normalization threshold. From the Bayes' theorem,

$$p(x|\mathcal{H}_s, \lambda, \Delta) = \frac{p(\Delta|x, \mathcal{H}_s, \lambda)p(x|\mathcal{H}_s, \lambda)}{p(\Delta|\mathcal{H}_s, \lambda)}, \quad (20)$$

where

$$p(\Delta|x, \mathcal{H}_s, \lambda) = p(x \geq x_{\text{th}}|x, \mathcal{H}_s, \lambda) = \begin{cases} 0 & x < x_{\text{th}}, \\ 1 & x \geq x_{\text{th}}, \end{cases} \quad (21)$$

and

$$p(\Delta|\mathcal{H}_s, \lambda) = p(x \geq x_{\text{th}}|\mathcal{H}_s, \lambda) = \int_{x_{\text{th}}}^{\infty} dx p(x|\mathcal{H}_s, \lambda). \quad (22)$$

Therefore, it is found that $p(x|\mathcal{H}_s, \lambda, \Delta)$ is normalized over the range in which x satisfies the detection criteria, while $p(x|\mathcal{H}_s, \lambda)$ is normalized over the entire range of possible values of x (when considering the log-LR of GstLAL, $x = \ln \mathcal{L}$, $-\infty \leq \ln \mathcal{L} \leq \infty$). The same goes for $p(x|\mathcal{H}_n)$ and $p(x|\mathcal{H}_n, \Delta)$. The probability described in (22) represents the fraction of detectable signals, and corresponds to the selection function, $\alpha(\lambda)$, in the previous studies [21, 33, 43]. It generally depends on the population parameters λ , and therefore accounts for selection effects when inferring them.

We have now identified three essential ingredients required to compute the hierarchical likelihood:

- the single-candidate likelihood under the background hypothesis: $p(x|\mathcal{H}_n, \Delta)$ and
- the single-candidate likelihood under the signal hypothesis: $p(x|\mathcal{H}_s, \lambda, \Delta)$.

In the following two subsections describe in turn how each of these ingredients can be modeled.

D. Single-candidate likelihood under the background hypothesis: $p(x|\mathcal{H}_n, \Delta)$

The PDF of the ranking statistic for noise-originating candidates, $p(x|\mathcal{H}_n)$, is among the data products produced by a detection pipeline, and used for FAR determination [35, 36, 47]:

$$\text{FAR}(x) = \frac{M \int_x^{\infty} dx' p(x'|\mathcal{H}_n, \Delta)}{T}, \quad (23)$$

where the factor, M , in (23) is the number of noise-like candidates with the detection statistic above the normalization threshold of $p(x|\mathcal{H}_n, \Delta)$. Considering the case of $x = \ln \mathcal{L}$, $p(x|\mathcal{H}_n) = p(\ln \mathcal{L}|\mathcal{H}_n)$ is obtained by integrating the GstLAL noise model for all n parameters over $n - 1$ dimensional surfaces of constant $\ln \mathcal{L}$ [36, 45]. Since the forms of the surfaces of constant $\ln \mathcal{L}$ is not

Algorithm 1: Noise model marginalization

```

for  $i \leftarrow 1$  to  $N_{\text{sample}}$  do
  Draw a sample from the proposal:  $\Theta_i \sim p(\Theta)$ ;
  Compute  $x \leftarrow \ln \mathcal{L}(\Theta_i)$ ;
  Update histogram:  $h_{\text{noise}}(x) + = p(\Theta_i | \mathcal{H}_n)/p(\Theta_i)$ ;

```

known, the integrals are approximated using importance-weighted sampling (See [45, Section IV] for detail). The procedure can be summarized as follows:

Regarding the fidelity of the GstLAL noise model, previous studies have shown good agreement between the model and the observed candidates distribution in the low-LR (or low-IFAR) region [38, 48, 49], although they diverge in high-LR region because of the presence of astrophysical signals.

E. Single-candidate likelihood under the signal hypothesis: $p(x|\mathcal{H}_s, \lambda)$

$p(x|\mathcal{H}_s, \lambda)$ is the likelihood of observing a ranking statistic value x under the assumption that the candidate originates from a GW signal produced by a CBC, with the source population described by the parameter λ . It can also be regarded as the PDF of the ranking statistic in the signal population. Unlike $p(x|\mathcal{H}_n)$ above, it is parameterized by λ . Thus, we need to model this PDF using the data products of the detection pipeline.

As described in Sec. II B, the GstLAL LR ranking statistic is determined by the n -dimensional parameter set describing each candidate, and is designed as a measure of how likely a given candidate is to be a GW signal from a CBC [35, 45–47]. Since the n -dimensional set includes the SNR and the best match template of the candidate of interest, in order to predict the distribution of the ranking statistic in the signal population, we need to assume the astrophysical and cosmological population models, which describe the distribution of the intrinsic parameters (masses, spins, etc.) and the luminosity distances of compact binaries. In the GstLAL signal model, the CBC rate is assumed to scale with the cube of the luminosity distance (in the local universe, this is equivalent to a uniform distribution in comoving volume) [45], and the model of the CBC intrinsic parameters distribution (*mass model*) is given by the analyst. In principle, the true population model is unknown—it is what we aim to learn from GW observations. Thus, any population model adopted within GstLAL cannot be correct in a strict sense. Nevertheless, assuming some form of population model is an essential step in the detection process.

The parameterization of the population model employed in the GstLAL signal model may differ from the parameterization we wish to use in population analysis; even if the same parameterization is adopted, the population parameters are fixed to specific values. Therefore, in order to perform population inference, we must repa-

parameterize the GstLAL signal model in a way that aligns with our objectives. It can be done as follows:

$$p(x|\mathcal{H}_s, \lambda) = \int d\rho_{\text{comb}} d\bar{\theta} p(x, \rho_{\text{comb}}, \bar{\theta}|\mathcal{H}_s, \lambda) \quad (24)$$

$$= \int d\rho_{\text{comb}} d\bar{\theta} p(x|\rho_{\text{comb}}, \bar{\theta}, \mathcal{H}_s, \lambda) p(\rho_{\text{comb}}, \bar{\theta}|\mathcal{H}_s, \lambda) \quad (25)$$

$$= \int d\rho_{\text{comb}} d\bar{\theta} p(x|\rho_{\text{comb}}, \bar{\theta}, \mathcal{H}_s) p(\rho_{\text{comb}}, \bar{\theta}|\mathcal{H}_s, \lambda). \quad (26)$$

where ρ_{comb} denotes the combined SNR of a network, and is defined by

$$\rho_{\text{comb}} = \sqrt{\sum_{\rho \in \tilde{\rho}} \rho^2}. \quad (27)$$

The second term in (26), $p(\rho_{\text{comb}}, \bar{\theta}|\mathcal{H}_s, \lambda)$, determined by the sensitivity of the instruments of interest and the assumed population model (The discussion in [50, Chapter 3] might be useful). The first term in (26) depends only on the characteristic of the search pipeline. It can be written as:

$$p(x|\rho_{\text{comb}}, \bar{\theta}, \mathcal{H}_s) = \frac{p(x, \rho_{\text{comb}}, \bar{\theta}|\mathcal{H}_s)}{\int dx p(x, \rho_{\text{comb}}, \bar{\theta}|\mathcal{H}_s)}, \quad (28)$$

and the joint distribution of the log-LR ranking statistic, the combined SNR and the best-matched template, $p(x, \rho_{\text{comb}}, \bar{\theta}|\mathcal{H}_s)$, is obtained by marginalizing GstLAL signal model. The marginalization can be done in the same sampling loop shown in Algorithm 1:

Algorithm 2: Noise and signal model marginalization

```

for  $i \leftarrow 1$  to  $N_{\text{sample}}$  do
  Draw a sample from the proposal:  $\Theta_i \sim p(\Theta)$ ;
  Compute  $x \leftarrow \ln \mathcal{L}(\Theta_i)$ ;
  Update histogram:  $h_{\text{noise}}(x) += p(\Theta_i | \mathcal{H}_n)/p(\Theta_i)$ ;
  Compute  $\rho_{\text{comb}} \leftarrow \rho_{\text{comb}}(\tilde{\rho}_i)$ ;
  Update histogram:
   $h_{\text{signal}}(x, \rho_{\text{comb}}, \bar{\theta}_i) += p(\Theta_i | \mathcal{H}_s)/p(\Theta_i)$ ;

```

Through the method described above, we can in principle replace the mass model and the spatial distribution model employed in the GstLAL signal model with the population model which we wish to use. However, in the importance-weighted sampling procedure, increasing the dimensionality of the target distribution requires a larger number of effective samples, which in turn leads to a higher computational cost. Since the primary aim of this work is not to obtain a scientifically meaningful estimate of cosmological parameters from real data, but rather to demonstrate the effectiveness of the proposed method, we perform the mock data analysis in an idealized setting in Sec. III. Specifically, we assume that the true intrinsic parameters distribution of compact binaries is already perfectly known and that the mass model

in the GstLAL signal model is set to be consistent with the true distribution. Under this assumption, there is no need to replace the mass model in the detection pipeline. The reparameterization in (26) then simplifies:

$$p(x|\mathcal{H}_s, \lambda) = \int d\rho_{\text{comb}} p(x, \rho_{\text{comb}}|\mathcal{H}_s, \lambda) \quad (29)$$

$$= \int d\rho_{\text{comb}} p(x|\rho_{\text{comb}}, \mathcal{H}_s, \lambda) p(\rho_{\text{comb}}|\mathcal{H}_s, \lambda) \quad (30)$$

$$= \int d\rho_{\text{comb}} p(x|\rho_{\text{comb}}, \mathcal{H}_s) p(\rho_{\text{comb}}|\mathcal{H}_s, \lambda). \quad (31)$$

The first term in (31), $p(x|\rho_{\text{comb}}, \mathcal{H}_s)$, denotes the likelihood that a ranking statistic value x is assigned to a candidate with combined (network) SNR, ρ_{comb} . It is a conditional probability distribution incorporating the characteristics of the detection pipeline, which can be obtained using the importance-weighted sampling procedure outlined above. The second term in (31) determined by the sensitivity of the instruments of interest, the mass distribution of CBC in the universe, and our cosmological model.

1. Modeling PDF of single detector SNR

In this subsection, we consider the calculation of the last term of (31) for a single detector case, $\rho_{\text{comb}} = \sqrt{\rho^2} = \rho$. We explicitly denote ρ as ρ_{obs} in this subsection to clarify that it refers to the observed SNR.

We define the optimal SNR, ρ_{opt} , as the expected SNR of a GW from a CBC which is optimally oriented and located to maximize the strain amplitude at a given detector. When we denote the redshift and the set of intrinsic source parameters that determine the value of ρ_{opt} by z and θ , respectively, the last term of (31) can be written as:

$$p(\rho_{\text{obs}}|\mathcal{H}_s, \lambda) = \int d\theta dz p(\rho_{\text{obs}}, \theta, z|\mathcal{H}_s, \lambda) \quad (32)$$

$$= \int d\theta dz p(\rho_{\text{obs}}|\theta, z, \mathcal{H}_s, \lambda) p(\theta, z|\mathcal{H}_s, \lambda) \quad (33)$$

$$= \int d\theta dz p(\rho_{\text{obs}}|\rho_{\text{opt}}(\theta, z, \lambda_c), \mathcal{H}_s) \times p(\theta|\mathcal{H}_s, \lambda_m) p(z|\mathcal{H}_s, \lambda_c). \quad (34)$$

The first term of (34) depends on the cosmological parameters, λ_c , and on our cosmological model thorough the conversion from redshift to luminosity distance. In addition, since ρ_{obs} here is the observed SNR, it should incorporate the measurement uncertainty of SNR caused by detector noise realization and the randomness of the sky location and orbital inclination of the source. The second term of (34) is determined by the astrophysical population. The third term can be constructed either on the basis of our cosmological model or, as commonly done in previous studies, using existing galaxy catalogues [9–16].

2. Measurement uncertainty of SNR

As mentioned above, the SNR of a GW signal from a compact binary source, characterized by a specific intrinsic parameter and a redshift, should scatter randomly around the optimal SNR, ρ_{opt} , defined earlier. This randomness arises from the realization of instrument noise as well as from the random sky location and inclination angle of the source, and such uncertainties must be incorporated into the first term of (34). In what follows, we examine how this uncertainty can be incorporated into the first term of (34), and how that term can be expressed more explicitly in terms of the optimal SNR, ρ_{opt} .

First, we consider the randomness caused by instrumental noise. As described in the section 7.8.1 of [51], matched filtering algorithms for CBC have traditionally filtered the data against a set of complex template, and the observed SNR, ρ_{obs} , is defined as the modulus of the complex SNR. When we assume the zero-mean stationary Gaussian noise and normalized templates, the real and imaginary part of the complex SNR become unit-variance Gaussian random variables [51, Section 7.2.4]. Therefore, under these assumptions, the distribution of the squared observed SNR, $X_{\text{obs}} \equiv \rho_{\text{obs}}^2$, becomes the non-central χ^2 distribution with two degrees of freedom [52]:

$$p(X_{\text{obs}}|\mathcal{H}_s, \nu) = \frac{1}{2} e^{-\frac{X_{\text{obs}} + \nu}{2}} I_0(\sqrt{\nu X_{\text{obs}}}), \quad (35)$$

where ν is the non-centrality parameter which is related to the expected value of the X_{obs} , and I_0 is the modified Bessel function of the first kind of order zero. When X_{exp} denotes the expected value of X_{obs} ,

$$X_{\text{exp}} = 2 + \nu. \quad (36)$$

It is reasonable to assume that

$$X_{\text{exp}} = (\rho_{\text{opt}} \mathcal{G})^2, \quad (37)$$

where \mathcal{G} is defined as the geometry factor of the instrument expressed as:

$$\mathcal{G} = \sqrt{F_+(\vec{n}, \psi)^2 \left(\frac{1 + \cos^2 \iota}{2} \right) + F_\times(\vec{n}, \psi)^2 \cos^2 \iota}. \quad (38)$$

Here, ι is the orbital inclination, and F_+ and F_\times are the antenna pattern functions [51]. They are determined by the unit vector, \vec{n} , pointing to the location of the CBC source on the sky and the polarization angle, ψ . From

$$p(\rho_{\text{obs}}) d\rho_{\text{obs}} = p(X_{\text{obs}}) dX_{\text{obs}} = 2\rho_{\text{obs}} p(X_{\text{obs}}) d\rho_{\text{obs}}, \quad (39)$$

we find that the first term of (34) can be written as:

$$p(\rho_{\text{obs}}|\rho_{\text{opt}}, \mathcal{H}_s) = \int_0^1 d\mathcal{G} p(\rho_{\text{obs}}, \mathcal{G}|\rho_{\text{opt}}, \mathcal{H}_s) \quad (40)$$

$$= \int_0^1 d\mathcal{G} p(\rho_{\text{obs}}|\mathcal{G}, \rho_{\text{opt}}, \mathcal{H}_s) p(\mathcal{G}|\mathcal{H}_s) \quad (41)$$

$$= \int_0^1 d\mathcal{G} p(\mathcal{G}|\mathcal{H}_s) \times 2\rho_{\text{obs}} p(X_{\text{obs}} = \rho_{\text{obs}}^2|\mathcal{H}_s, \nu = (\rho_{\text{opt}} \mathcal{G})^2 - 2). \quad (42)$$

The last term of (42) can be calculated using (35), and the first term, $p(\mathcal{G}|\mathcal{H}_s)$, can be obtained from simulation assuming a uniform and isotropic distribution of gravitational wave sources.

As shown in Fig. 1, in the high-SNR limit the distribution, $p(\rho_{\text{obs}}|\mathcal{G}, \rho_{\text{opt}}, \mathcal{H}_s)$, in (41) and (42) approaches a Gaussian distribution, $p(\rho_{\text{obs}}|\mu, \sigma) = \frac{1}{\sqrt{2\pi\sigma^2}} \exp[-(x - \mu)^2/2\sigma^2]$, with the mean of $\mu = \rho_{\text{opt}} \mathcal{G}$ and the unit variance, $\sigma = 1$. Even at $\rho_{\text{opt}} \mathcal{G} \simeq 4$, the mean-squared error is only about 0.1%. Motivated by this, in the MDAs presented in Sec. III, we simplify the treatment by replacing $p(\rho_{\text{obs}}|\mathcal{G}, \rho_{\text{opt}}, \mathcal{H}_s)$ with the unit-variance Gaussian distribution:

$$p(\rho_{\text{obs}}|\rho_{\text{opt}}, \mathcal{H}_s) \simeq \int_0^1 d\mathcal{G} p(\mathcal{G}|\mathcal{H}_s) \mathcal{N}(\rho_{\text{obs}}|\rho_{\text{opt}} \mathcal{G}, 1). \quad (43)$$

3. PDF of combined SNR

In this subsection, for simplicity, we assume a detector network composed of multiple instruments with nearly identical sensitivities—such as the two LIGO detectors. Under this assumption, we show how to construct the distribution of the combined SNR from the single detector SNR distribution and the distribution of the relative magnitude of geometry factors of different instruments. Although in reality some candidates are observed by only a subset of the N_{inst} instruments, for simplicity we assume that all candidates in our dataset D are identified by all N_{inst} detectors and examine the corresponding distribution of the combined SNR.

Then, for now, it is assumed that we have $N_{\text{inst}} = m + 1$ instruments (m is an integer equal to or greater than 1), and we already know the distribution of SNRs observed by the 0th instrument, O_0 , for the given value of cosmological parameters, $p(\rho_0|\mathcal{H}_s, \lambda)$. When the ratio of SNR observed by 0th and i th instruments for a given source is written as

$$r_{i,0} \equiv \frac{\rho_i}{\rho_0}, \quad (44)$$

the combined SNR defined by (27) can be expressed as

$$\rho_{\text{comb}} = \rho_0 \sqrt{1 + \sum_{i=1}^m r_{i,0}^2}. \quad (45)$$

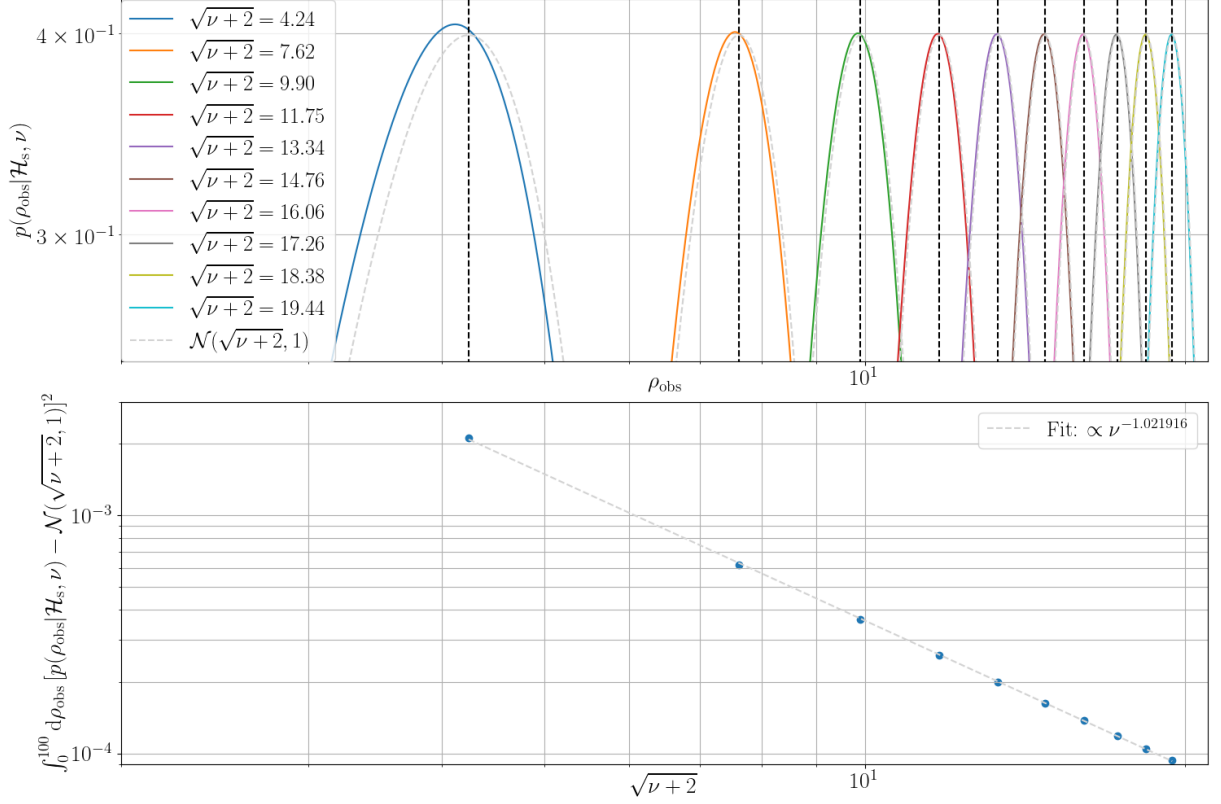


FIG. 1. Comparison between the unit-variance Gaussian distribution, $\mathcal{N}(\rho_{\text{obs}}|\sqrt{\nu+2}, 1)$, and the expected distribution of the observed SNR ρ_{obs} , $p(\rho_{\text{obs}}|\mathcal{H}_s, \nu)$, derived from the non-central chi-squared distribution, conditioned by the non-centrality $\nu = (\rho_{\text{opt}}\mathcal{G})^2 - 2$. *Top panel:* the two distributions are shown for different value of ν ; the colored solid lines represent the exact $p(\rho_{\text{obs}}|\mathcal{H}_s, \nu)$, while the gray dashed lines represent the unit-variance Gaussian distributions. The two distributions converge in the high-SNR limit. *Bottom panel:* the mean-squared error between $p(\rho_{\text{obs}}|\mathcal{H}_s, \nu)$ and the unit-variance Gaussian distribution as a function of $\sqrt{\nu+2} = \rho_{\text{opt}}\mathcal{G}$, showing an $\sim \nu^{-1}$ scaling.

Considering

$$p(\rho_0, r_{1,0}, \dots, r_{m,0}) d\rho_0 \prod_{i=1}^m dr_{i,0} = p(\rho_{\text{comb}}, r_{1,0}, \dots, r_{m,0}) d\rho_{\text{comb}} \prod_{i=1}^m dr_{i,0} \quad (46)$$

and

$$d\rho_{\text{comb}} = \left(\sqrt{1 + \sum_{i=1}^m r_{i,0}^2} \right) d\rho_0, \quad (47)$$

we obtain

$$\begin{aligned} p(\rho_{\text{comb}}|\mathcal{H}_s, \lambda) &= \int \left(\prod_{i=1}^m dr_{i,0} \right) p(\rho_{\text{comb}}, r_{1,0}, \dots, r_{m,0}|\mathcal{H}_s, \lambda) \quad (48) \\ &= \int \left(\prod_{i=1}^m dr_{i,0} \right) \frac{1}{\sqrt{1 + \sum_{i=1}^m r_{i,0}^2}} \\ &\quad \times p \left(\rho_0 = \frac{\rho_{\text{comb}}}{\sqrt{1 + \sum_{i=1}^m r_{i,0}^2}}, r_{1,0}, \dots, r_{m,0} \middle| \mathcal{H}_s, \lambda \right). \end{aligned} \quad (49)$$

Since the distribution of $r_{i,0}$ depends roughly only on the geometric properties of the instrument network and does not depend on cosmological parameters or astrophysical mass distribution models, the last term in (49) can be factorized as follows:

$$p(\rho_0, r_{1,0}, \dots, r_{m,0}|\mathcal{H}_s, \lambda) = p(\rho_0|\mathcal{H}_s, \lambda) p(r_{1,0}, \dots, r_{m,0}|\mathcal{H}_s). \quad (50)$$

When the sensitivity of two detectors are very similar, the ratio of the SNRs between them is nearly equal to the ratio of their geometry factors,

$$r_{i,0} \simeq \frac{\mathcal{G}_i}{\mathcal{G}_0}. \quad (51)$$

Accordingly, the approximated distribution of $r_{i,0}$ can be obtained by computing the geometry factors for each instrument over a set of isotropically distributed sky locations and uniformly distributed inclinations, and taking their ratios.

F. Point estimate of signal fraction

This subsection details the procedure for obtaining a point estimate of the signal fraction, $\bar{\eta}$, which was mentioned around (7). Recalling (14), the signal fraction can be written using the probability of astrophysical origin, $p(\mathcal{H}_s|x, \lambda, \bar{\eta}, \Delta)$, so-called $p(\text{astro})$:

$$\bar{\eta} = p(\mathcal{H}_s|\lambda, \bar{\eta}, \Delta) = \int dx p(\mathcal{H}_s|x, \lambda, \Delta) p(x|\lambda, \bar{\eta}, \Delta). \quad (52)$$

Here we define $p(x|\text{observed})$ as the observed distribution of the detection statistic, and using the true value of the signal fraction $\bar{\eta}_0$ it can be written as

$$p(x|\text{observed}) = \bar{\eta}_0 p(x|\mathcal{H}_s, \lambda, \Delta) + (1 - \bar{\eta}_0) p(x|\mathcal{H}_n, \Delta), \quad (53)$$

if our population model is correct and the total number of observed candidates N_{tot} is sufficiently large. Assuming

$$p(x|\lambda, \bar{\eta}, \Delta) \simeq p(x|\text{observed}), \quad (54)$$

we obtain an approximation of the signal fraction, and we refer to it as $\bar{\eta}'_1$:

$$\bar{\eta} \simeq \int dx p(\mathcal{H}_s|x, \lambda, \bar{\eta}, \Delta) p(x|\text{observed}) \quad (55)$$

$$\simeq \frac{1}{N_{\text{tot}}} \sum_{i=1}^{N_{\text{tot}}} p(\mathcal{H}_s|x_i, \lambda, \Delta) \equiv \bar{\eta}'_1, \quad (56)$$

Since the calculation of $p(\mathcal{H}_s|x, \lambda, \bar{\eta}, \Delta)$ requires us to know $\bar{\eta}$ as shown later, we approximate $p(\mathcal{H}_s|x, \lambda, \bar{\eta}, \Delta)$ in (55) with the $p(\text{astro})$ marginalized over $\bar{\eta}$:

$$p(\mathcal{H}_s|x, \lambda, \Delta) = \int_0^1 d\bar{\eta} p(\mathcal{H}_s, \bar{\eta}|x, \lambda, \Delta) \quad (57)$$

$$= \int_0^1 d\bar{\eta} p(\mathcal{H}_s|x, \lambda, \bar{\eta}, \Delta) p(\bar{\eta}|\lambda, \Delta). \quad (58)$$

From Bayes' theorem,

$$p(\mathcal{H}_s|x, \lambda, \bar{\eta}, \Delta) = \frac{p(\mathcal{H}_s|\lambda, \bar{\eta}, \Delta) p(x|\mathcal{H}_s, \lambda, \Delta)}{p(\mathcal{H}_s|\lambda, \bar{\eta}, \Delta) p(x|\mathcal{H}_s, \lambda, \Delta) + p(\mathcal{H}_n|\lambda, \bar{\eta}, \Delta) p(x|\mathcal{H}_n, \Delta)} \quad (59)$$

$$= \frac{\bar{\eta} p(x|\mathcal{H}_s, \lambda, \Delta)}{\bar{\eta} p(x|\mathcal{H}_s, \lambda, \Delta) + (1 - \bar{\eta}) p(x|\mathcal{H}_n, \Delta)}. \quad (60)$$

$p(x|\mathcal{H}_n, \Delta)$ and $p(x|\mathcal{H}_s, \lambda, \Delta)$ is the PDF of the detection statistic in the noise and signal population, and these are described in the previous subsections. We adopt the uniform prior between 0 and 1 as $p(\bar{\eta}|\lambda, \Delta)$.

If N_{tot} is sufficiently large and the approximation in (54) holds well, the fraction of signals is expected to be estimated with adequate accuracy using (56) (as well as (58) and (60)). In the MDAs in Sec. III, however, we find that this approximation does not work well especially in the case of the smaller injected values of $\bar{\eta}$, and moreover that the resulting discrepancy can have a serious impact on the posterior distribution of the population parameters, which is the final outcome of our analysis. On the other hand, we also found that the true signal fraction, $\bar{\eta}_0$, and $\bar{\eta}'_1$ in (56) are related by a linear relation:

$$\bar{\eta}'_1 \simeq (F - B)\bar{\eta}_0 + B, \quad (61)$$

where

$$F(\lambda, \Delta) \equiv \int_{-\infty}^{\infty} dx p(\mathcal{H}_s|x, \lambda, \Delta) p(x|\mathcal{H}_s, \lambda, \Delta) \quad (62)$$

and

$$B(\lambda, \Delta) \equiv \int_{-\infty}^{\infty} dx p(\mathcal{H}_s|x, \lambda, \Delta) p(x|\mathcal{H}_n, \Delta). \quad (63)$$

The linear relation in (61) can be readily derived by substituting (53) into (55). We define the point estimate corrected using the relation in (61) as

$$\bar{\eta}'_0 \equiv \frac{\bar{\eta}'_1 - B}{F - B}. \quad (64)$$

The discovery of the relation in (61) enables us to obtain more accurate estimates of the signal fraction from the observational dataset, which can then be incorporated into the inference of the population parameter. The comparison between the results of inferences employing different methods of estimation of signal fraction is shown in Sec. III D 3.

As may already be apparent from the preceding discussion, the order of presentation above reflects the heuristic path by which we arrived at the estimator in (64), rather than the minimal conceptual structure required to understand it. In fact, for the conceptual understanding of the estimator, the probabilistic derivation in (52) and (55) is not essential. What truly underlies the estimator is the fact that the expectation value of any function of the detection statistic differs between the signal and noise populations, and that the observed mean reflects a mixture of the two according to the true signal fraction. The $p(\text{astro})$ -based formulation simply provides a convenient and interpretable way to express this relation, and this choice was also empirically justified in our MDA, as discussed in Sec. III D.

III. PROOF-OF-CONCEPT MOCK DATA ANALYSES

In this section, we validate our proposed method by performing simplified, proof-of-concept MDAs. In our proof-of-concept MDAs, we did not inject signals into detector strain and run the detection pipeline to generate a list of GW candidates. Instead, we drew fixed numbers of ranking statistic values corresponding to candidates from our noise and signal models, respectively, and used this synthetic (fake) dataset to compute the posterior distribution of H_0 . Accordingly, in a MDA our dataset consists of a list of N_{tot} values of the log-likelihood ratio. Assuming that all population parameters other than the Hubble constant, H_0 , are known, we investigate whether the injection value of H_0 can be recovered from a dataset consisting of N_{tot} fake candidates. We use the data products generated in the S5S6 reanalysis [53] for the fake data generation and the construction of the single-candidate likelihood under the signal/noise hypothesis.

The population model employed in our MDAs and the single-candidate likelihood under the signal hypothesis based on it are described in Sec. III A. Sec. III B describes our fake data generation process. In Sec. III D, we show the example posterior and the results of the probability-probability (p-p) test.

A. Population model

To perform the p-p test, we prepared 1,386 mock universes, corresponding to 126 different values of the Hubble constant H_0 and 11 different values of the signal fraction $\bar{\eta}$. For consistency with the prior described in Sec. II A, H_0 is varied uniformly from $25 \text{ km s}^{-1} \text{ Mpc}^{-1}$ to $150 \text{ km s}^{-1} \text{ Mpc}^{-1}$ in increments of $1 \text{ km s}^{-1} \text{ Mpc}^{-1}$, $\bar{\eta}$ was sampled uniformly from 0 to 1 with a step size of 0.1.

We begin by describing the CBC intrinsic parameter distribution in the mock universes, which corresponds to the second term of (34). For simplicity, we consider only the lowest post-Newtonian order. At this level, the optimal SNR defined in Sec. II E 1 depends only on the detector frame chirp mass, \mathcal{M}_c , and the luminosity distance between the source and the Earth, d_L : $\rho_{\text{opt}} = \rho_{\text{opt}}(\mathcal{M}_c, d_L)$. The source frame and the detector frame chirp mass is defined as:

$$M_c = \left(\frac{m_{1,s}^3 m_{2,s}^3}{m_{1,s} + m_{2,s}} \right)^{\frac{1}{5}}, \quad (65)$$

and

$$\mathcal{M}_c = (1+z)M_c = \left(\frac{m_{1,d}^3 m_{2,d}^3}{m_{1,d} + m_{2,d}} \right)^{\frac{1}{5}}, \quad (66)$$

where $m_{1,s}$ and $m_{2,s}$ are the source-frame masses of the binary components ($m_{1,s} \geq m_{2,s}$), and $m_{1,d} = (1+z)m_{1,s}$

and $m_{2,d} = (1+z)m_{2,s}$ are the detector-frame masses of the binary components. Defining $\mathcal{M}_{c,8}$ and $d_{L,8}$ such that $\rho_{\text{opt}}(\mathcal{M}_{c,8}, d_{L,8}) = 8$, we can calculate ρ_{opt} for a given set of values of chirp mass and luminosity distance as:

$$\rho_{\text{opt}}(\mathcal{M}_c, d_L) = 8 \left(\frac{\mathcal{M}_c}{\mathcal{M}_{c,8}} \right)^{5/6} \frac{d_{L,8}}{d_L}. \quad (67)$$

$\mathcal{M}_{c,8}$ and $d_{L,8}$ depend on the sensitivity of the instrument of interest. Our MDAs used the power spectral density estimated from a segment of LIGO Hanford data in S5, spanning GPS times 866736411–875232014. The reference distance $d_{L,8}$ for a given $\mathcal{M}_{c,8}$ was computed using the `gstlal.psd.HorizonDistance` function in the GstLAL package [47], which evaluates the horizon distance for a binary with specified component masses and detector power spectral density. Accordingly, in this setting, the only intrinsic parameter of the binary that controls the optimal SNR is the chirp mass in the source frame, M_c . This implies that the second term in (34) can be expressed as:

$$p(\theta|\mathcal{H}_s, \lambda_m) = p(M_c|\mathcal{H}_s, \lambda_m). \quad (68)$$

In typical population studies of GW sources, it is common to assume a source-frame mass distribution motivated by astrophysical considerations as in (34). In our MDAs, however, we choose to fix the mass distribution in the detector frame to maintain consistency with the run configuration used in [53], whose data products are used in this study. Since the focus of our MDAs is not on extracting redshift information from features in the mass distribution, this choice is not important. Considering $p(\mathcal{M}_c|z, \mathcal{H}_s, \lambda_m) = \frac{1}{(1+z)}p(M_c|\mathcal{H}_s, \lambda_m)$, (34) can be rewritten as:

$$p(\rho_{\text{obs}}|\mathcal{H}_s, \lambda) = \int d\mathcal{M}_c dz p(\rho_{\text{obs}}|\rho_{\text{opt}}(\mathcal{M}_c, d_L(z, \lambda_c)), \mathcal{H}_s) \times p(\mathcal{M}_c|z, \mathcal{H}_s, \lambda_m)p(z|\mathcal{H}_s, \lambda_c). \quad (69)$$

The binary detector-frame component masses are assumed to be log-uniformly distributed in the mock universes. The mass range is set to be $1\text{--}100 M_\odot$ for the detector-frame component masses and up to $100 M_\odot$ for the detector-frame total mass. Then, we obtained $p(\mathcal{M}_c|z, \mathcal{H}_s, \lambda_m)$ numerically by drawing samples of $m_{1,d}$ and $m_{2,d}$ from $p(m) \propto 1/m$, and calculating (66) for each sample.

We now turn to the third term of (34). In the mock universes, compact binaries are uniformly distributed in the comoving volume, V_c . Therefore,

$$p(z|\mathcal{H}_s, \lambda_c) \propto \frac{T}{1+z} \frac{dV_c}{dz}, \quad (70)$$

where T is the length of the observation in the detector frame ($T/(1+z)$ is the length of the observation in

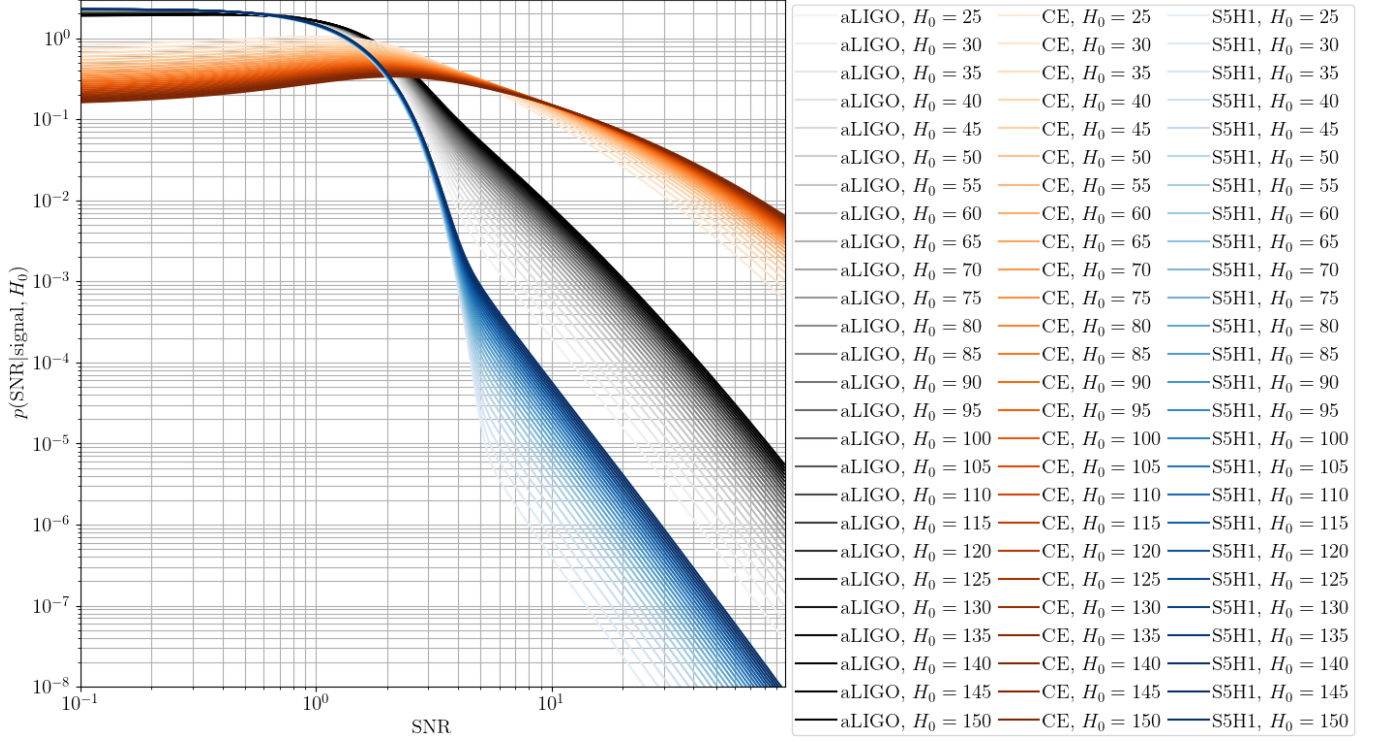
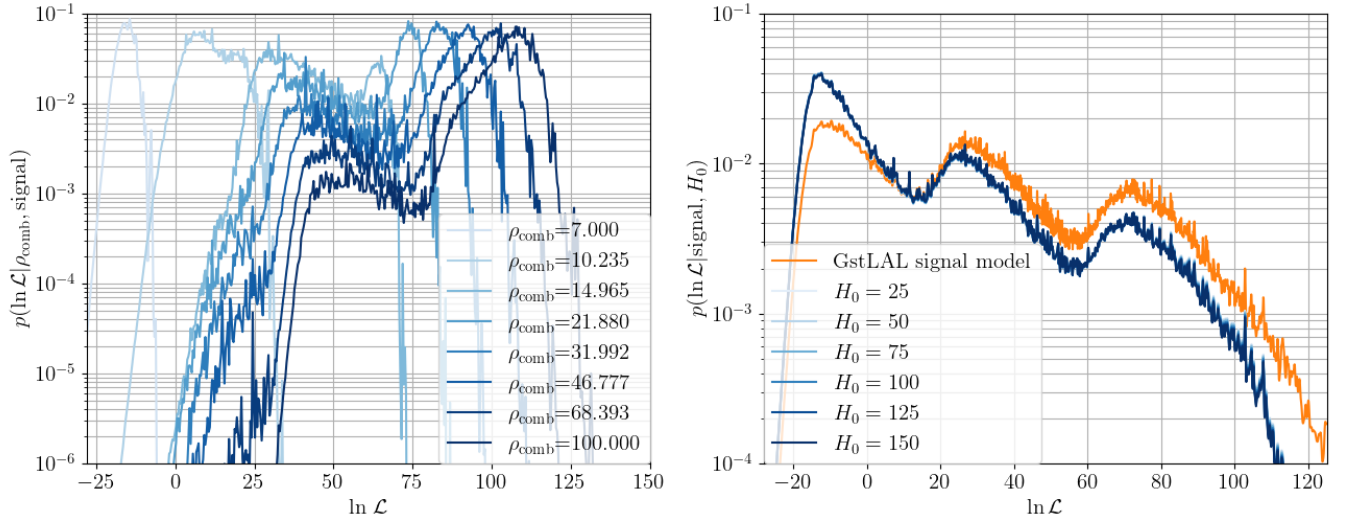
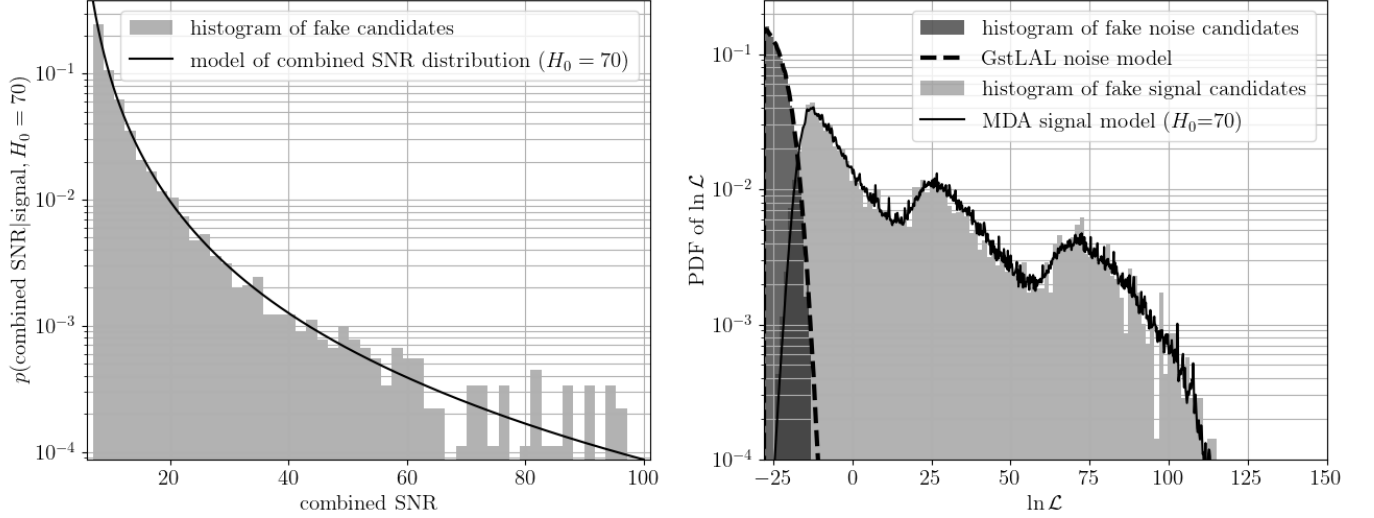


FIG. 2. Expected SNR distribution assuming a given instrument and the population model described in Sec. III A. The gray lines, orange lines and blue lines correspond to Cosmic Explorer [54], Advanced LIGO design sensitivity [55], and S5 sensitivity, spanning GPS time 866736411–875232014, respectively.



(a) $\ln \mathcal{L}$ distribution model under the signal hypothesis conditioned by observed SNR, obtained by marginalizing GstLAL signal model assuming S5 sensitivity via importance sampling described in Algorithm 2. (b) $\ln \mathcal{L}$ distribution model under the signal hypothesis for a given value of H_0 , obtained by integrating the results shown by blue lines in Fig. 2 and Fig. 3a. As a reference, the original marginalized GstLAL signal model is plotted in orange.

FIG. 3. Detection statistic distribution models employed in the MDA. These PDFs were generated based on data products provided by a previous study [53]. The H_0 -dependence of this MDA signal model remains limited, since the LIGO detectors during the S5 run were not sensitive to very distant regions of the universe.



(a) The combined SNR distribution of the signal-originating candidates in an example MDA dataset. The black solid line shows the network SNR distribution model corresponding to the injected value of H_0 , $H_0 = 70 \text{ km s}^{-1} \text{ Mpc}^{-1}$, as a reference.

(b) The log-LR distribution of the candidates in an example MDA dataset. The black dashed line presents the GstLAL noise model, and the black solid line shows the MDA signal model corresponding to the injected value of H_0 , $H_0 = 70 \text{ km s}^{-1} \text{ Mpc}^{-1}$.

FIG. 4. Comparison between the distribution models, and the distribution of candidates' SNR and log-LR in an example MDA dataset.

the source frame). Furthermore, the mock universes are “flat”. Then the expressions of the comoving distance, d_C , and the luminosity distance, d_L , as a function of the redshift, z , are:

$$d_C(z, \lambda_c) = \int_0^z dz' \frac{c}{H(z', \lambda_c)} \quad (71)$$

and

$$d_L(z, \lambda_c) = (1+z)d_C(z, \lambda_c), \quad (72)$$

where c denotes the speed of the light, $\lambda_c = \{H_0, \Omega_m\}$ and

$$H(z, \lambda_c) = H_0 \sqrt{\Omega_m(1+z)^3 + 1 - \Omega_m}. \quad (73)$$

We use the fixed value of the fractional matter density in the MDA, $\Omega_m = 0.3$. Considering

$$\frac{dV_c}{dz} = \frac{d}{dz} \frac{4\pi}{3} d_C^3 = 4\pi d_C^2 \frac{dd_C}{dz} = 4\pi d_C(z, \lambda_c)^2 \frac{c}{H(z, \lambda_c)}, \quad (74)$$

we obtain

$$p(z|\mathcal{H}_s, \lambda_c) \propto \frac{1}{1+z} \frac{d_C(z, \lambda_c)^2}{H(z, \lambda_c)}. \quad (75)$$

Putting (66), (67), (68), (71), (72), (73) and (75) into (34), we obtain the observed SNR distribution model for a given instrument. The SNR distribution model shown by the blue lines in Fig. 2 assumes the sensitivity of the LIGO Hanford detector during the period from GPS time 866736411–875232014, and it is employed in the MDAs.

For comparison, the gray lines and the orange lines in Fig. 2 show the SNR distribution models assuming the Advanced LIGO design sensitivity [55] and the Cosmic Explorer design sensitivity [54], respectively. The dependence of the distribution shape on the value of H_0 tends to be more pronounced in the low-SNR region, and it can be seen that the better the assumed detector sensitivity—enabling distant CBC to be observed with higher SNR—the stronger the H_0 -dependence of the distribution shape becomes.

By applying the importance sampling procedure described in Algorithm 2, we obtained the distribution of the ranking statistic conditioned on a given SNR, corresponding to the first term of (31) (shown in Fig. 3a). The importance sampling was performed on the Kam-bai cluster at the Research Center for the Early Universe (RESCEU), The University of Tokyo. Each node of the cluster is equipped with an Intel Xeon E5-2630 v4 CPU (20 threads) and 32 GB of memory. The main computation consisted of 60 independent jobs with comparable computational cost. The total wall time amounted to 637.9 hours (equivalent to 26.6 node-days) and the total CPU time to 3695.7 hours (user 3681.8 h, system 13.9 h). The average peak memory usage per job was 31.7 GB, with a maximum of 39.4 GB. In this study, for simplicity—as described in the first paragraph of Sec. II E 3—we impose as part of our detection criteria that all candidates included in our candidate list must be coincident across all detectors in the network (specifically, both the LIGO Hanford (H1) and LIGO Livingston (L1) detectors in our MDAs). Accordingly, in Algorithm 2, if a sample drawn from the proposal distribu-

tion corresponds to the set of instruments \bar{O} other than $\{H1, L1\}$, such as $\bar{O} = \{H1\}$ or $\bar{O} = \{L1\}$, the signal model histogram h_{signal} is not updated and the loop proceeds to the next iteration. Since the primary goal of this work is to validate the proposed framework, we did not invest significant effort in optimizing this part of the implementation. As a result, the PDFs are likely to have converged less efficiently than what could be achieved with a more optimized implementation, given the computational resources expended.

Furthermore, using the single-detector SNR distribution model shown by blue lines in Fig. 2 together with the method described in Sec. II E 3, we constructed a two-detector combined SNR distribution model (assuming the Hanford and Livingston detectors with the identical sensitivity). By integrating these results thorough (31), we obtained the single-candidate likelihood model under the signal hypothesis for different H_0 , as shown in Fig. 3b. As a reference, the original GstLAL signal model is plotted in orange, allowing a visual assessment of how the replacement of the spatial distribution model—described in Sec. II E—affects the resulting distribution of the detection statistic. As mentioned above, the LIGO detectors during the S5 run were not sensitive to very distant regions of the universe. Consequently, the H_0 -dependence of the model of the ranking statistic PDF under the signal hypothesis remains limited. We refer to the H_0 -dependent distribution model of the detection statistic for astrophysical, signal-originating candidates, constructed through the process described so far, as the MDA signal model.

B. Data generation

We have used the inverse transform sampling to generate our synthetic dataset. The noise candidates are drawn from the GstLAL noise model, and the signal candidates drawn from the combined SNR distribution model. Noise candidates are drawn directly from the PDF model of the ranking statistic, subject to the requirement $-28 \leq \ln \mathcal{L} \leq 150$, and the data-generation process ends there. For signal candidates, we first draw two-detector combined SNR values from the SNR distribution model constructed using S5 sensitivity, which corresponds to the injection value of H_0 , subject to the requirement $7 \leq \text{SNR} \leq 100$. This lower SNR threshold is imposed because the GstLAL software assigns a ranking statistic of negative infinity to triggers with network SNR below 7. Given the SNR of each candidate, we then draw ranking statistic values from the conditional distribution, $p(x|\rho_{\text{comb}}, \mathcal{H}_s, \lambda)$, shown in Fig. 3a. For also signal-originating candidates, we include only those satisfying $-28 \leq \ln \mathcal{L} \leq 150$ in the dataset. This selection corresponds to the detection criteria, Δ , introduced in the formalism section, Sec. II. While in the section Δ was defined solely by a lower threshold on the detection statistic, here we also impose an upper threshold for prac-

tical convenience in normalizing probability distribution. This additional restriction has no impact on the formalism itself.

By applying (23) together with the actual counts of candidates observed between GPS times 866736411–875232014, we obtain the IFAR corresponding to the lower and upper detection thresholds, $\ln \mathcal{L} = -28$ and $\ln \mathcal{L} = 150$, as 42 seconds and 1.4×10^{72} years, respectively. This demonstrates that our method is capable of handling catalogues that include candidates spanning a very broad range of statistical significance.

Although it is possible to generate signal candidates directly from the PDF of the ranking statistic (the MDA signal model), we chose not to do so, as this would obscure the connection to quantities such as SNR that readers may find more intuitive. A dataset based on component masses and redshifts would be even closer to astrophysical reality, but given the scope of this work we adopted a simpler, more tractable approach. Fig. 4 shows the comparison between the example of the distribution of synthetic candidates and the modeled distributions.

In each mock universe, 10,000 candidates were generated. The numbers of signal-originating and noise-originating candidates were determined so as to be consistent with the value of $\bar{\eta}$ assigned to each mock universe.

C. Fidelity test of the signal fraction point estimate

To further assess the fidelity of the signal fraction point estimation method described in Sec. II F, we conducted a dedicated validation test using a separate set of mock universes, distinct from the 1,386 mock universes used in the main MDAs. This validation set consists of 1,500 mock universes, with injected values of $\bar{\eta}$ uniformly distributed between 0 and 1 in steps of $\Delta\bar{\eta} = 2/1500$, while the Hubble constant H_0 is fixed at $70 \text{ km s}^{-1} \text{ Mpc}^{-1}$ for all. The data generation procedure follows the same approach as described in Sec. III B. For universes with injected $\bar{\eta} < 0.5$, we use a common list of 150,000 noise-origin candidates (ranking statistics), while only the signal-origin candidates vary across universes; the total number of candidates is not preserved. Conversely, for injected $\bar{\eta} > 0.5$, a common list of 150,000 signal-origin candidates is used, and only the noise-origin candidates differ between universes. Again, the total number of candidates is not preserved.

D. Results and interpretations

1. Results from joint estimate of H_0 and $\bar{\eta}$

We performed a joint estimation of H_0 and $\bar{\eta}$ for each of the mock universes corresponding to 126 different values of H_0 and 11 different values of $\bar{\eta}$, using the synthetic observational data generated in Sec. III B. Fig. 5 presents 24 of the resulting 1,386 posteriors for H_0 . Each row

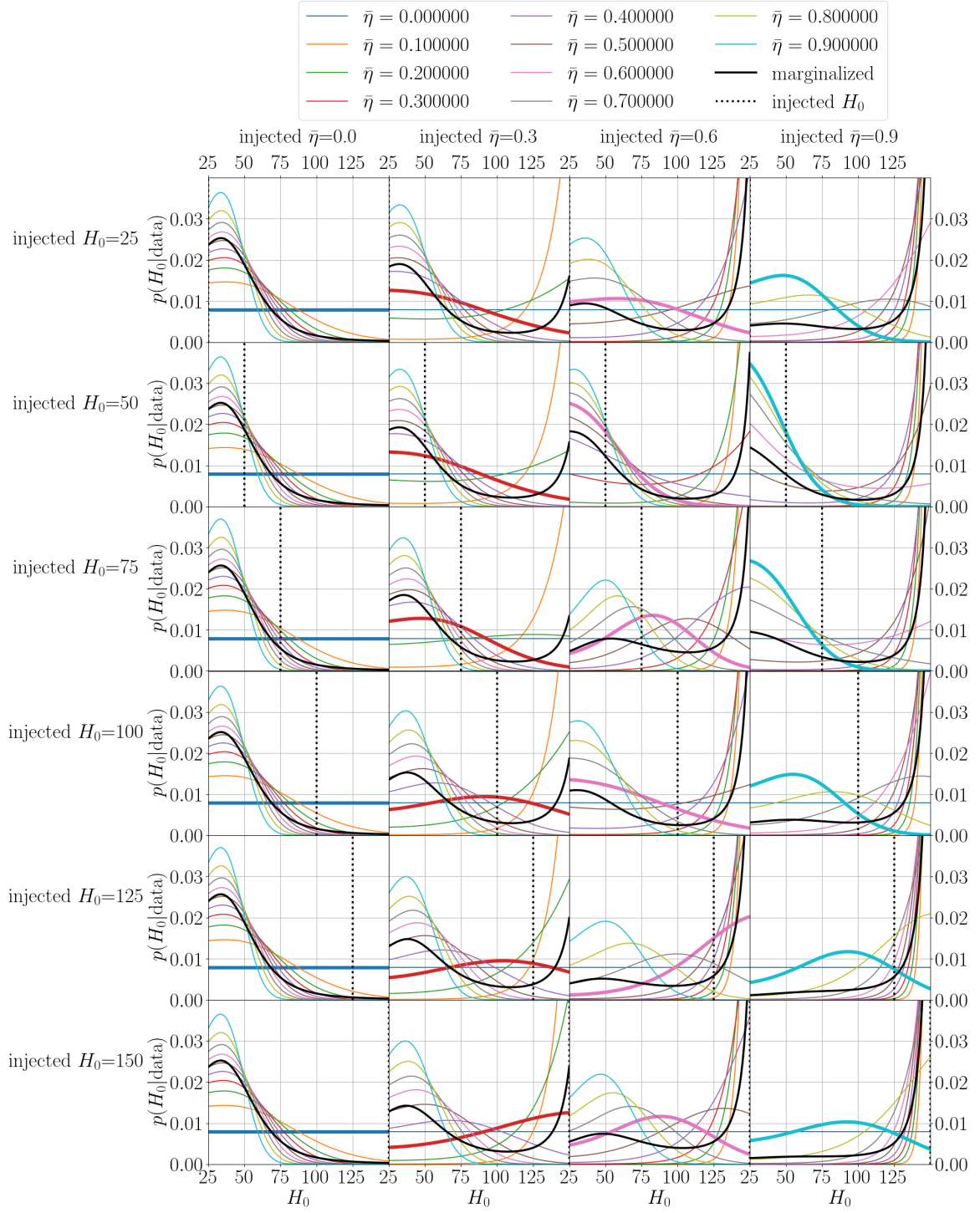


FIG. 5. Posteriors marginalized over the signal fraction, $\bar{\eta}$, from MDAs with different injected values of the Hubble constant H_0 and the signal fraction $\bar{\eta}$. Each row corresponds to a group of mock universes with different injected values of H_0 , while each column corresponds to those with different injected values of $\bar{\eta}$. In each panel, the black solid line shows the posterior of H_0 marginalized over $\bar{\eta}$, whereas the colored lines show the posteriors of H_0 calculated under different assumed values of $\bar{\eta}$. The curve corresponding to the true (injected) value of $\bar{\eta}$ for each mock universe is drawn with a thicker line, and the black dotted line indicates the true (injected) value of H_0 . When $\bar{\eta} = 0$ is assumed in the evaluation of the posteriors (in the case of blue lines in each panel), no constraint on H_0 is obtained. The marginalized posteriors show little sensitivity to the injected H_0 values, compared to their dependence on the injected $\bar{\eta}$ values. In contrast, the posteriors obtained using the true $\bar{\eta}$ tend to track the injected H_0 values reasonably well.

corresponds to a group of mock universes with different injected values of H_0 , while each column corresponds to those with different injected values of $\bar{\eta}$. In each panel, the black solid line shows the posterior of H_0 marginalized over $\bar{\eta}$, whereas the colored lines show the posteriors of H_0 calculated under different assumed values of $\bar{\eta}$. The curve corresponding to the true (injected) value of $\bar{\eta}$ for each mock universe is drawn with a thicker line, and the black dotted line indicates the true (injected) value of H_0 . Although only ten colored lines are shown, corresponding to $\bar{\eta}$ values from 0 to 0.9 in steps of 0.1, in each mock universe we actually computed the H_0 posterior for 1,000 $\bar{\eta}$ values between 0 and 1, which were subsequently marginalized. As expected, when $\bar{\eta} = 0$ is assumed in the evaluation of the posteriors (in the case of blue lines in each panel), all the candidates in our datasets are interpreted as noise, and thus no constraint on H_0 is obtained. From a global perspective, the marginalized posteriors (black solid lines) show little sensitivity to the injected H_0 values, compared to their dependence on the injected $\bar{\eta}$ values. This is consistent with the discussion in the previous subsection and with Fig. 3b: because the sensitivity of the initial LIGO detector in the S5 era was not sufficient to probe distant sources, the shape of the ranking statistic distribution is only weakly dependent on H_0 . In contrast, the posteriors obtained using the true $\bar{\eta}$ tend to track the injected H_0 values reasonably well. This behavior motivates the use of a point estimate of $\bar{\eta}$ based on $p(\text{astro})$, as introduced in Sec. II F.

Fig. 6 shows the p-p plot obtained from the analyses of 1,386 mock universes. The blue line shows the fraction of mock universes whose injected H_0 values fall within a given credible interval (C.I.) of the inferred posterior. The credible intervals are calculated in a one-sided (left-tailed) manner. The shaded region indicates the 90% confidence interval expected from the binomial distribution. To quantify deviations from uniformity, we performed a Kolmogorov-Smirnov (KS) test using SciPy's `kstest` function [56], yielding a p -value of ~ 0.1 . While some deviation from the confidence band is observed, no significant inconsistency is found between the recovered posteriors and the injected values.

2. Results of fidelity test of $\bar{\eta}$ point estimate

Fig. 7 presents the results of the signal fraction fidelity test described in Sec. III C. In the main panel, the horizontal axis shows the true (injected) signal fraction $\bar{\eta}_0$, while the vertical axis shows the signal fraction estimated using our point estimate method based on $p(\text{astro})$. The black dashed line represents the ideal relation in which the estimated value exactly matches the true value. The thick light gray solid line shows the relationship between $\bar{\eta}_0$ and the estimated value $\bar{\eta}'_1$, obtained as a simple sum of $p(\text{astro})$ values divided by the total number of candidates as described in (56). While this line is linear like the ideal case, its slope differs, and it intersects the ideal

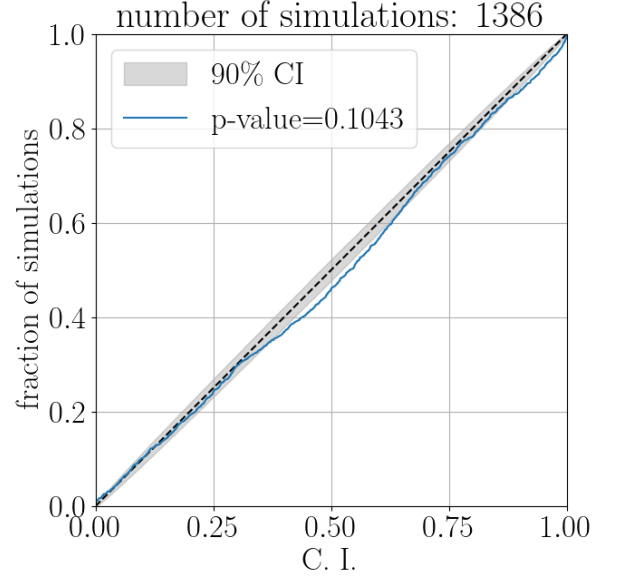


FIG. 6. Probability-probability plot for the joint estimate of H_0 and $\bar{\eta}$, derived from the analyses of 1,386 mock universes, corresponding to 126 different values of the Hubble constant H_0 and 11 different values of the signal fraction $\bar{\eta}$. The shaded region indicates the 90% confidence interval expected from the binomial distribution and the p -value shown in the legend is obtained from KS test [56]. While some deviation from the confidence band is observed, no significant inconsistency is found between the recovered posteriors and the injected values.

diagonal near $\bar{\eta}_0 = 0.5$. The upper subpanel shows the corresponding relative error $|\bar{\eta}'_1 - \bar{\eta}_0|/\bar{\eta}_0$ as a light gray solid line. The error decreases near $\bar{\eta}_0 = 0.5$ and increases toward the edges of the plot; in particular, it exceeds 100% for small values of $\bar{\eta}_0$. The dark gray dotted line in the main panel indicates the corrected estimate $\bar{\eta}'_0$ obtained using (64), which closely follows the ideal relation. The upper subpanel shows the corresponding relative error $|\bar{\eta}'_0 - \bar{\eta}_0|/\bar{\eta}_0$ as a dark gray dotted line, revealing that the error decreases as $\bar{\eta}_0$ increases. For $\bar{\eta}_0 \gtrsim 0.03$, the corrected estimate achieves better than 5% accuracy, and the error drops below 1% near $\bar{\eta}_0 = 1$. The blue solid line in the main panel is a least-squares fit to the linear relationship between $\bar{\eta}_0$ and $\bar{\eta}'_1$, with the best-fit parameters shown in the legend. The orange dashed line represents the linear prediction based on (61), and its coefficients are also indicated in the legend. This predicted relationship agrees well with the observed trend (light gray solid line and blue fit). This agreement, in turn, enables the accurate correction illustrated by the dark gray dotted line.

As briefly mentioned in the end of Sec. II F, from the conceptual point of view of the point estimation, it is not necessary to use $p(\text{astro})$. In principle, one could construct an analogous estimator by replacing $p(\text{astro})$, $p(\mathcal{H}_s|x, \lambda, \Delta)$ in (56), (62) and (63) with any function of the detection statistic, such as the detection statistic

x itself. However, when we performed the same fidelity test using this replacement, the relative error showed a similar monotonic decrease with $\bar{\eta}_0$ but remained larger overall: the error did not fall below 1% even near $\bar{\eta}_0 = 1$, and the true signal fraction needed for the error to drop below 5% was $\bar{\eta}_0 \gtrsim 0.1$. These results empirically justify our choice of employing $p(\text{astro})$ in the estimator.

3. Results using point estimate of signal fraction

Fig. 9 shows a set of 11 p-p plots, each corresponding to a group of 126 mock universes sharing the same injected value of $\bar{\eta}$. The analyses in each panel are based on the Dirac delta prior introduced in (7). In general, any mismatch between the population distribution used to generate the simulations and the prior assumed in Bayesian inference appears as a bias in the resulting p-p plot. However, as confirmed in Sec. IIID2, the difference between our estimate $\bar{\eta}'$ and the injected value $\bar{\eta}_0$ is small, at least in the case of $\bar{\eta}' = \bar{\eta}'_0$, that we can approximate $\delta(\bar{\eta} - \bar{\eta}') \simeq \delta(\bar{\eta} - \bar{\eta}_0)$, and thereby construct p-p plots for each value of the injected $\bar{\eta}$ (or $\bar{\eta}_0$). In each of 11 panels, the gray shaded region represents the 90% frequentist confidence band, same as in Fig. 6. The blue solid and orange dashed lines indicate the results of the p-p tests assuming $\bar{\eta}' = \bar{\eta}'_1$ and $\bar{\eta}' = \bar{\eta}'_0$, respectively. The green dotted lines will be discussed later. The results shown in the panels corresponding to small injected values of $\bar{\eta}$, specifically $\bar{\eta} \lesssim 0.2$, behave as expected. The orange dashed lines lie close to the diagonal, and the associated KS test p-values (shown in the same color) are near unity. In contrast, for injected $\bar{\eta} = 0$ and 0.1, the blue solid lines deviate substantially from the diagonal due to large discrepancies between the estimate $\bar{\eta}'_1$ and the injected value, resulting in small KS p-values. As anticipated from the results in Fig. 7, the blue curves become progressively better as the injected $\bar{\eta}$ approaches 0.5, eventually showing similar behavior to the orange dashed curves. For the injected $\bar{\eta} \gtrsim 0.3$, both the blue solid and orange dashed lines begin to deviate noticeably from the diagonal. Ideally, we would expect the orange dashed lines to remain close to the diagonal for all the injected values of $\bar{\eta}$ while the blue solid lines should show strong deviations for the injected $\bar{\eta} \simeq 0.9$ and 1—similar in magnitude to the deviations seen for the injected $\bar{\eta} = 0$ and 0.1. However, this expected pattern is not observed. We hypothesize that the fact that both the blue and orange curves exhibit similarly strong biases in the mock universes with large injected $\bar{\eta}$ indicates the presence of a systematic error that has not been accounted for in our previous explanations. This systematic effect appears to dominate over the differences between $\bar{\eta}'_0$ and $\bar{\eta}'_1$. We attribute its origin to the lack of sufficient convergence in our MDA signal model constructed via importance sampling, which results in residual statistical fluctuations in the modeled signal distribution.

In our main MDAs, the same non-converged MDA sig-

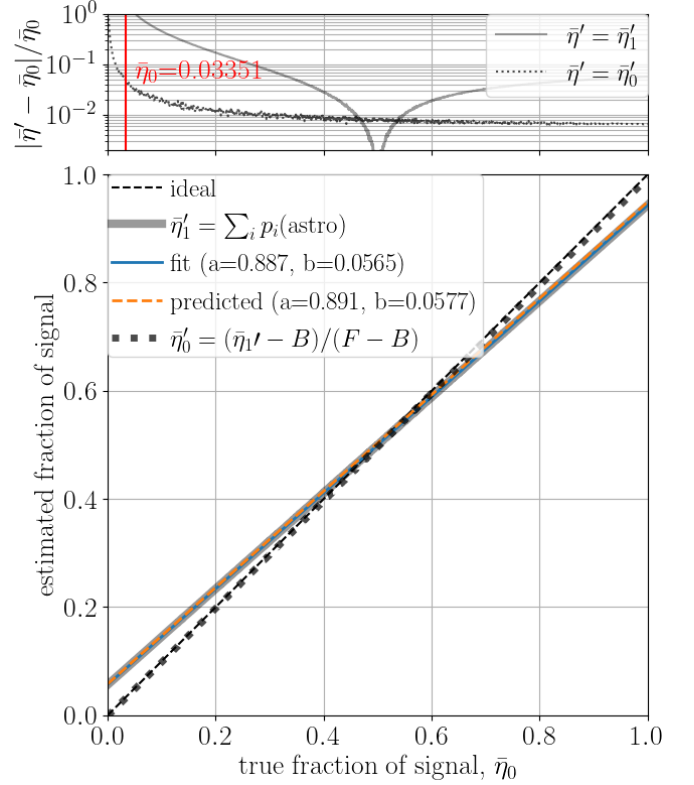


FIG. 7. True signal fraction vs. estimated signal fraction. In the bottom main panel, the horizontal axis shows the injected signal fraction $\bar{\eta}_0$, while the vertical axis shows the signal fraction estimated using our point estimate method based on $p(\text{astro})$. The upper subpanel shows the relative estimation error $|\bar{\eta}' - \bar{\eta}_0|/\bar{\eta}_0$. For the estimator defined in (56), $\bar{\eta}'_1$, the error decreases near $\bar{\eta}_0 = 0.5$ and increases toward the edges of the plot; it exceeds 100% for small values of $\bar{\eta}_0$. For the estimator defined in (64), $\bar{\eta}'_0$, the error decreases as $\bar{\eta}_0$ increases. For $\bar{\eta}_0 \gtrsim 0.03$, $\bar{\eta}'_0$ achieves better than 5% accuracy, and the error drops below 1% near $\bar{\eta}_0 = 1$.

nal model—with residual statistical fluctuations—is used both in data generation and in the evaluation of the hierarchical likelihood. However, since data generation is inherently stochastic, we expect that the impact of fluctuations in the MDA signal model is relatively minor in this step: synthetic candidate lists drawn from the noisy signal model are likely to be similar to those drawn from a fully converged model. In contrast, the hierarchical likelihood evaluation is more sensitive to such fluctuations, and we hypothesize that this asymmetry is responsible for the biases observed in many of the p-p plots shown in Fig. 9.

To prepare for a mathematical explanation of the bias introduced in the evaluation of the hierarchical likelihood due to statistical fluctuations in the MDA signal model, we begin by defining two detection-statistic probability density models. The true, fully converged, fluctuation-

free model is defined, following (19), as:

$$p_{\text{true}}(x|H_0, \bar{\eta}) = \bar{\eta} p_{\text{true}}(x|\mathcal{H}_s, H_0) + (1 - \bar{\eta}) p_{\text{true}}(x|\mathcal{H}_n). \quad (76)$$

The fluctuation-affected model, constructed via importance sampling using a finite number of samples, is denoted as:

$$\hat{p}(x|H_0, \bar{\eta}) = p_{\text{true}}(x|H_0, \bar{\eta}) + \bar{\eta} \epsilon(x|H_0), \quad (77)$$

where $\epsilon(x|H_0)$ characterizes the statistical fluctuation present primarily in the signal component (the MDA signal model). This modeling is motivated by the empirical observation (see Fig. 4b) that the noise model exhibits much smaller fluctuations than the signal model. Even if there are small residual fluctuations in the noise component, they are independent of H_0 and thus do not affect the relative likelihood between different H_0 values. Therefore, we neglect the contribution of fluctuations from the noise model and model the total PDF fluctuation using only the signal-side variation scaled by $\bar{\eta}$. In our practical implementation, we evaluate the logarithmic form of the hierarchical likelihood. For a fluctuation-free model, this takes the form:

$$\ln p_{\text{true}}(D|H_0, \bar{\eta}) = \sum_{i=1}^{N_{\text{tot}}} \ln p_{\text{true}}(x_i|H_0, \bar{\eta}). \quad (78)$$

In contrast, when using the fluctuation-affected model, the likelihood becomes:

$$\ln \hat{p}(D|H_0, \bar{\eta}) = \sum_{i=1}^{N_{\text{tot}}} [\ln p_{\text{true}}(x_i|H_0, \bar{\eta}) + \bar{\eta} \epsilon(x_i|H_0)] \quad (79)$$

$$= \ln p_{\text{true}}(D|H_0, \bar{\eta}) + \sum_{i=1}^{N_{\text{tot}}} \ln \left[1 + \frac{\bar{\eta} \epsilon(x_i|H_0)}{p_{\text{true}}(x_i|H_0, \bar{\eta})} \right]. \quad (80)$$

Denoting the ensemble average over the realization of the importance-sampled model as $\langle \cdot \rangle$, and assuming $\left\langle \frac{\bar{\eta} \epsilon(x|H_0)}{p_{\text{true}}(x|H_0, \bar{\eta})} \right\rangle = 0$, from the Maclaurin expansion to the leading order, we obtain

$$\left\langle \ln \left[1 + \frac{\bar{\eta} \epsilon(x_i|H_0)}{p_{\text{true}}(x_i|H_0, \bar{\eta})} \right] \right\rangle \simeq -\frac{1}{2} \left\langle \left[\frac{\bar{\eta} \epsilon(x|H_0)}{p_{\text{true}}(x|H_0, \bar{\eta})} \right]^2 \right\rangle. \quad (81)$$

Consequently, the expected log hierarchical likelihood evaluated with the fluctuation-affected model is always smaller than the true value:

$$\begin{aligned} & \langle \ln \hat{p}(D|H_0, \bar{\eta}) \rangle \\ & \simeq \ln p_{\text{true}}(D|H_0, \bar{\eta}) - \frac{1}{2} \sum_{i=1}^{N_{\text{tot}}} \left\langle \left[\frac{\bar{\eta} \epsilon(x_i|H_0)}{p_{\text{true}}(x_i|H_0, \bar{\eta})} \right]^2 \right\rangle \\ & \leq \ln p_{\text{true}}(D|H_0, \bar{\eta}). \end{aligned} \quad (82)$$

Therefore, if the magnitude of fluctuation varies with H_0 , this bias can lead to spurious suppression of the hierarchical likelihood at particular values of H_0 , independent of

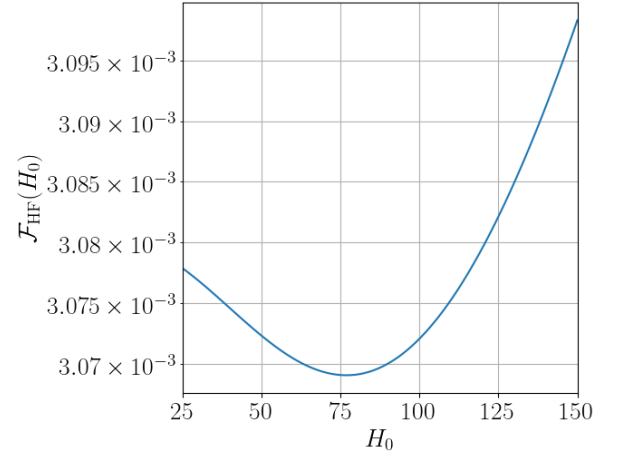


FIG. 8. The fraction of power contained in fluctuations with wavelengths shorter than the wavelength $\Delta x = \Delta \ln \mathcal{L} \leq 5$ of the detection statistic distribution, $p(x|\mathcal{H}_s, H_0)$, for each value of H_0 . It is observed that the signal models corresponding to larger values of H_0 have a greater fraction of high-frequency oscillation power.

their proximity to the injected truth. It can also be found that the systematic underestimation of the hierarchical likelihood becomes more severe as either $\bar{\eta}$ increases, or N_{tot} increases, since the second term of (82) increases monotonically with both variables.

To quantitatively evaluate the H_0 -dependence of the magnitude of statistical fluctuations in our MDA signal model, we computed the fraction of power contained in fluctuations with wavelengths shorter than the wavelength $\Delta x = \Delta \ln \mathcal{L} \leq 5$ of the detection statistic distribution, $p(x|\mathcal{H}_s, H_0)$, as defined below, for each value of H_0 :

$$\mathcal{F}_{\text{HF}}(H_0) \equiv \frac{\int_{f \geq 1/\Delta x} df |\tilde{p}(f|H_0)|^2}{\int_{f > 0} df |\tilde{p}(f|H_0)|^2}, \quad (83)$$

where $\tilde{p}(f|H_0)$ is the Fourier transform of $p(x|\mathcal{H}_s, H_0) - \bar{p}(H_0)$, and $\bar{p}(H_0)$ is the DC (zero-frequency) component of $p(x|\mathcal{H}_s, H_0)$. Fig. 8 shows the dependence of \mathcal{F}_{HF} on H_0 , computed for our MDA signal model. It is observed that the signal models corresponding to larger values of H_0 have a greater fraction of high-frequency oscillation power.

Fig. 10 shows a subset of the posteriors obtained from the MDAs assuming a Dirac delta prior. Focusing on the orange curves, which correspond to the case of injected $\bar{\eta} = 0.9$, we observe that the posteriors consistently exhibit suppression around large H_0 values, regardless of the injected value of H_0 . This behavior is consistent with the discussion leading up to (82) and with the trend in the magnitude of model fluctuations shown in Fig. 8. In contrast, the blue curves corresponding to injected $\bar{\eta} = 0.1$ show no such suppression, supporting the interpretation from (82) that the systematic underestimation of the hierarchical likelihood becomes more

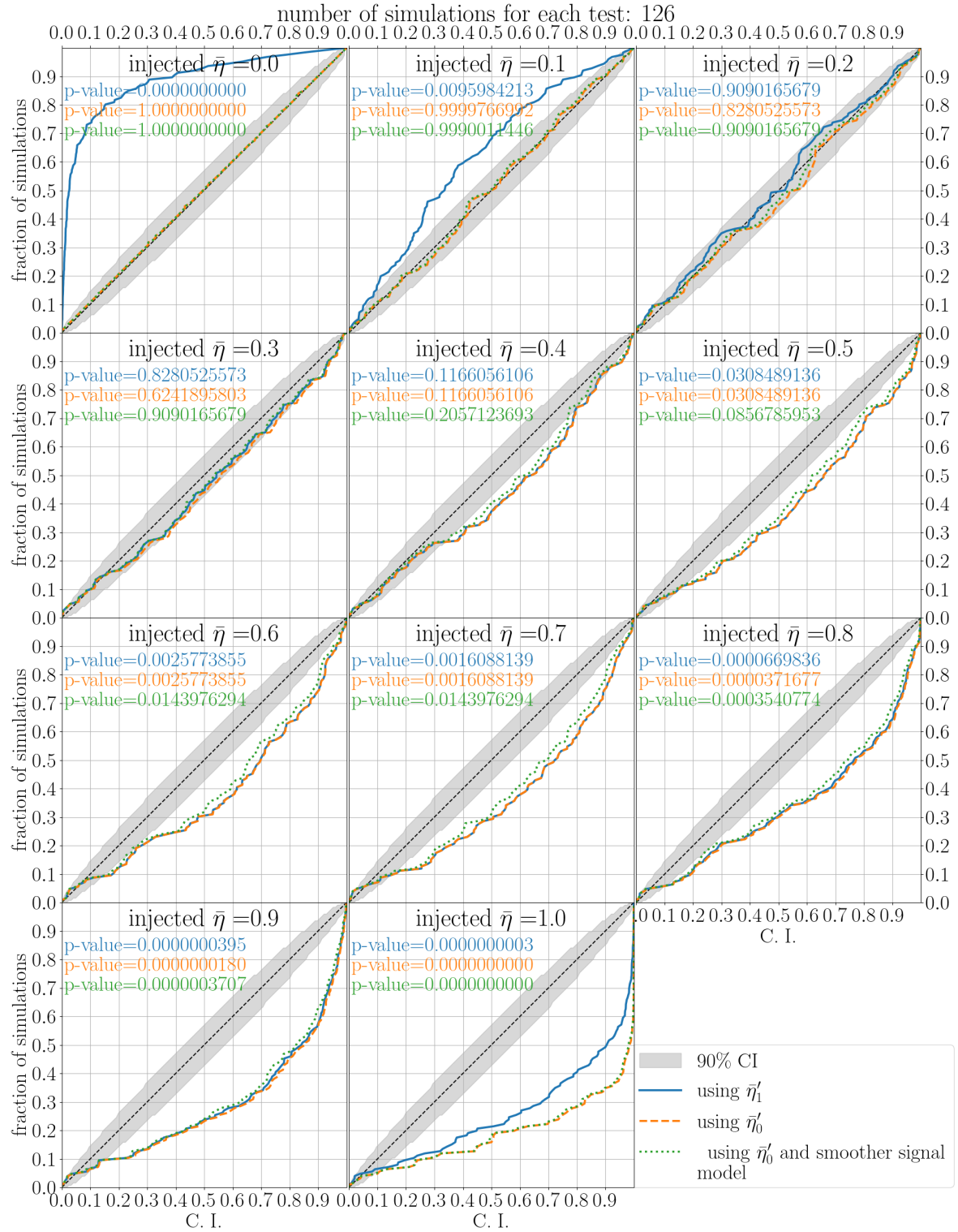


FIG. 9. Probability-probability plots for the inferences using the point estimate of the signal fraction $\bar{\eta}$ with different injection values of $\bar{\eta}$. In each of 11 panels, the gray shaded region represents the 90% frequentist confidence band, same as in Fig. 6. The blue solid and orange dashed lines indicate the results of the p-p tests assuming $\bar{\eta}' = \bar{\eta}'_1$ and $\bar{\eta}' = \bar{\eta}'_0$, respectively. The green dotted lines represents the p-p plot derived from the smoother signal model, calculated via importance sampling using 4 times as many samples as the MDA signal model shown in Fig. 3b. For injected values of $\bar{\eta} \lesssim 0.2$, we find that the Hubble constant can be inferred without noticeable bias when using a reliable signal fraction estimator. In contrast, for $\bar{\eta} \gtrsim 0.3$, the impact of underestimation of the hierarchical likelihood at specific H_0 values, induced by the H_0 -dependent fluctuation of the MDA signal model, becomes significant.

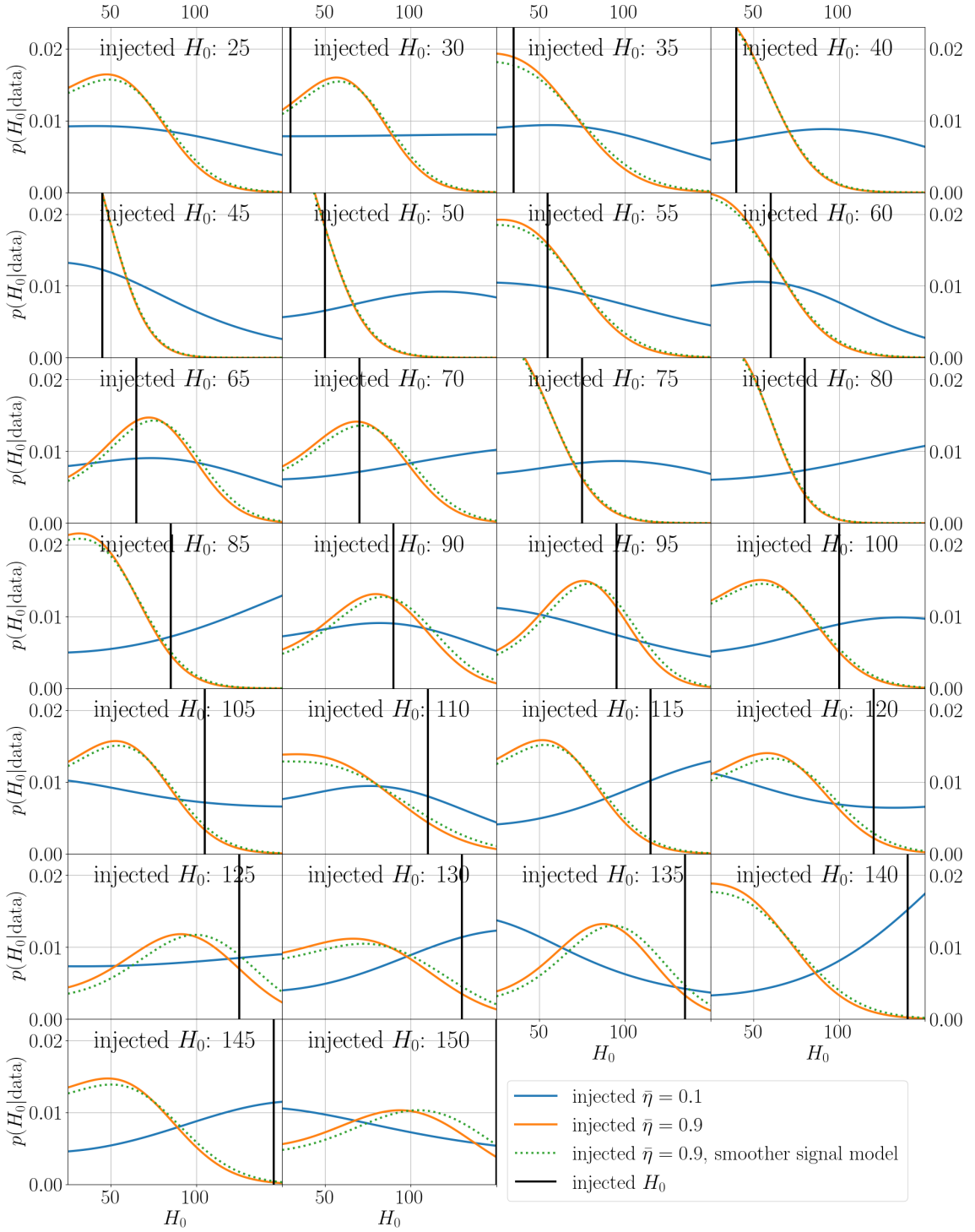


FIG. 10. Comparison of the posteriors obtained using the point estimate of the signal fraction, between the different injection value of the signal fraction, $\bar{\eta} = 0.1$ and 0.9 . The posteriors corresponding to the injected $\bar{\eta} = 0.9$, shown by orange lines, consistently exhibit suppression around large H_0 values, regardless of the injected value of H_0 . This behavior is consistent with the discussion leading up to (82) and with the trend in the magnitude of model fluctuations shown in Fig. 8. In contrast, the blue curves corresponding to injected $\bar{\eta} = 0.1$ show no such suppression, supporting the interpretation from (82) that the systematic underestimation of the hierarchical likelihood becomes more severe as $\bar{\eta}$ increases. The green dotted lines also show the posterior for the mock universe with the injected $\bar{\eta} = 0.9$, and the analyzed datasets are same as those of the orange lines. However, the posteriors shown by the green dotted lines obtained from the hierarchical likelihood evaluation using the smoother signal model than the original MDA signal model. When using a smoother signal model for the hierarchical likelihood evaluation, the suppression at large H_0 becomes relatively less pronounced.

severe as $\bar{\eta}$ increases. Furthermore, the suppression of the hierarchical likelihood at large H_0 implies that the resulting left-sided Bayesian credible intervals may be underestimated. This is consistent with the observation that the p-p plot in Fig. 6 and those for mock universe groups with $\bar{\eta} \gtrsim 0.3$ in Fig. 9 exhibit a systematic sagging below the diagonal. The green dotted line in Fig. 10 shows the posterior distribution obtained by analyzing mock data with injected $\bar{\eta} = 0.9$ using a different signal model from our original MDA signal model constructed in Sec. III A. The observed data (i.e., the GW candidate list) are exactly the same as those used for the orange solid lines. The difference lies in the signal model, which is slightly smoother because it was constructed via importance sampling using 4 times as many samples as the original model. Although the difference is subtle, the green dotted posteriors are consistently shifted toward larger H_0 values compared to the orange curves, which is consistent with our previous discussions. In addition, the green dotted lines in Fig. 9 represent the p-p plot derived from this smoother signal model. While the improvement is marginal, it lies slightly closer to the diagonal than the orange line.

IV. CONCLUSION

We have presented a Bayesian hierarchical framework for inferring population parameters from unedited compact object merger catalogues—i.e., candidates lists produced directly by a search pipeline, without the application of additional selection thresholds (e.g., $p(\text{astro}) \geq 0.5$) as typically used in GWTC catalogues [3–7]. Crucially, this framework does not require per-candidate parameter estimation and instead operates directly on the detection statistic values assigned to each candidate. Our approach is a practical variant of the general hierarchical inference framework developed by [30].

To validate the method, we applied it to a large number of mock datasets and focused on the joint inference of the Hubble constant H_0 and the signal fraction $\bar{\eta}$, relying on the data products generated in the S5S6 reanalysis [53]. The H_0 -dependence of the MDA signal model remains limited, since the LIGO detectors during the S5 run were not sensitive to very distant regions of the universe. Consequently, our MDAs mostly unable to recover the injected H_0 . However, the probability-probability test demonstrated that the recovered posteriors are statistically consistent with the injected values: the obtained p-p plot lies close to the diagonal, with a p-value of ~ 0.1 obtained from the KS test [56]. While a slight downward deviation from the diagonal is observed, it is consistent with the bias expected from the incomplete convergence of the MDA signal model discussed in Sec. III D 3. Although some convergence issue of the signal model remains, the overall result indicates that our inference framework itself is essentially free from bias, as evidenced by the p-p test. This outcome also substan-

tiates our initial expectation that, by using a dataset consisting of the detection statistics themselves, which already reflect the search threshold, the framework can naturally incorporate the selection imposed by the search without requiring explicit injection-based sensitivity estimates.

As a proof of concept, our MDAs were designed to highlight the conceptual structure of the framework rather than to achieve a fully realistic cosmological inference. To reduce computational cost and complexity, we assumed an idealized situation in which the true intrinsic parameter distribution of compact binaries is already perfectly known and is consistently used as the population model in the detection pipeline. Accordingly, our mock universes were constructed to follow the same mass model as adopted in the S5S6 reanalysis [53], namely a log-uniform distribution in the detector-frame mass. Our simplified assumption is not realistic, and furthermore, previous studies have highlighted the importance of jointly estimating the mass distribution and cosmological parameters to avoid biases [12, 13], as well as the potential improvement in precision when using more structured mass models featuring, for example, mass gaps or peaks [19, 57–60]. As discussed in Sec. II B, however, the detection statistic generated by a search pipeline is computed under a specific population model, and its distribution changes when the underlying population changes. In our implementation, we modified the GstLAL signal model and used it as the single-candidate likelihood under the signal hypothesis. If one were to jointly estimate cosmological and other population parameters, this modification could not be limited to replacing the SNR distribution model as done in (31), but would require a full modification of the signal model as described in (26). Even in our simplified MDAs, incomplete convergence of the signal model posed a problem, and such a full modification would further increase the dimensionality of the PDF estimated via importance-weighted sampling, making convergence more computationally demanding. Understanding how well the signal model needs to be converged in order to ensure unbiased inference will be an important topic for future study, particularly in the context of simultaneous estimation of multiple population parameters. Our results indicate that the bias arising from incomplete convergence tends to increase with the signal fraction and the total number of candidates, suggesting that achieving sufficient convergence will become increasingly critical for precision inference of cosmological or astrophysical population parameters in future analyses.

As a possible direction for addressing this convergence issue, we note that the importance-weighted sampling algorithm used to construct the signal model—adapted from the GstLAL programs [47]—was originally optimized for building the noise model rather than the signal model. As can be seen in Fig. 3a, the model looks smooth and well converged in the noise-like region with small $\ln \mathcal{L}$, while in the more signal-like region with large $\ln \mathcal{L}$,

it exhibits noticeable fluctuations. This suggests that the current algorithm efficiently extracts noise-like samples but is less effective for sampling signal-like events. Developing algorithms that can efficiently address this issue will be essential for future analyses that aim to extract maximal information from large GW datasets through joint estimation of population and cosmological parameters.

Although the joint inference of signal fraction and population parameters has been explored in earlier works [30, 33], our analyses emphasize that $\bar{\eta}$ can be separately estimated from the observational data using a method based on the average of $p(\text{astro})$. Specifically, we showed that a point estimate of $\bar{\eta}$, derived from the linearly transformed average of $p(\text{astro})$, closely matches the injected value. When this estimate is used to construct a Dirac delta prior for the signal fraction, the resulting population inferences—in our MDAs, constraints on H_0 —becomes more informative than those obtained from joint inference. We presented both the results of joint inference and the results obtained by fixing $\bar{\eta}$ to the point estimate. While the joint posteriors showed no significant bias, the Dirac-prior analyses yielded noticeably tighter constraints, confirming that leveraging a reliable signal fraction estimate enhances the informativeness of population-level inference.

While one of the main strengths of our framework lies in not requiring per-candidate parameter estimation—allowing us to handle catalogues consisting of a large number of candidates—this advantage inherently involves a trade-off between the breadth of information gained from many candidates and the depth of information obtainable from the detailed characterization of each candidate. It will therefore be an interesting subject for future studies to investigate, for detectors of various sensitivities and observation durations, under what conditions this method can achieve constraints on population parameters, including H_0 , that are comparable to those obtained with conventional population-inference method.

ACKNOWLEDGMENTS

The authors are grateful for computational resources provided by the LIGO Laboratory and supported by National Science Foundation grants PHY-0757058 and PHY-0823459. This research has made use of LALSuite software [61]. RH was supported by JST SPRING (JPMJSP2108). RH and KC were supported by JSPS KAKENHI grants JP18H03698 and JP23H04893. HF acknowledges support from the NSERC Alliance International Collaboration program.

-
- [1] B. F. Schutz, *Nature* **323**, 310 (1986).
 - [2] B. P. Abbott *et al.*, *Nature* **551**, 85–88 (2017).
 - [3] B. P. Abbott *et al.* (LIGO Scientific Collaboration and Virgo Collaboration), *Phys. Rev. X* **9**, 031040 (2019).
 - [4] R. Abbott *et al.* (LIGO Scientific Collaboration and Virgo Collaboration), *Phys. Rev. X* **11**, 021053 (2021).
 - [5] R. Abbott *et al.* (The LIGO Scientific Collaboration and the Virgo Collaboration), *Phys. Rev. D* **109**, 022001 (2024).
 - [6] R. Abbott *et al.* (LIGO Scientific Collaboration, Virgo Collaboration, and KAGRA Collaboration), *Phys. Rev. X* **13**, 041039 (2023).
 - [7] A. G. Abac *et al.*, “GWTC-4.0: Updating the Gravitational-Wave Transient Catalog with Observations from the First Part of the Fourth LIGO-Virgo-KAGRA Observing Run,” (2025), arXiv:2508.18082 [gr-qc].
 - [8] W. Del Pozzo, *Phys. Rev. D* **86**, 043011 (2012).
 - [9] M. Fishbach *et al.*, *Astrophys. J. Lett.* **871**, L13 (2019).
 - [10] M. Soares-Santos *et al.*, *Astrophys. J. Lett.* **876**, L7 (2019).
 - [11] R. Gray, I. M. Hernandez, H. Qi, A. Sur, P. R. Brady, H.-Y. Chen, W. M. Farr, M. Fishbach, J. R. Gair, A. Ghosh, D. E. Holz, S. Mastrogiovanni, C. Messenger, D. A. Steer, and J. Veitch, *Phys. Rev. D* **101** (2020), 10.1103/physrevd.101.122001.
 - [12] R. Abbott *et al.*, *Astrophys. J.* **949**, 76 (2023).
 - [13] T. L. S. Collaboration, the Virgo Collaboration, and the KAGRA Collaboration, “Gwtc-4.0: Constraints on the cosmic expansion rate and modified gravitational-wave propagation,” (2025), arXiv:2509.04348 [astro-ph.CO].
 - [14] A. Petiteau, S. Babak, and A. Sesana, *Astrophys. J.* **732**, 82 (2011).
 - [15] S. Mastrogiovanni, G. Pierra, S. Perriès, D. Laghi, G. C. Santoro, A. Ghosh, R. Gray, C. Karathanasis, and K. Leyde, “Icarogw: A python package for inference of astrophysical population properties of noisy, heterogeneous and incomplete observations,” (2023), arXiv:2305.17973 [astro-ph.CO].
 - [16] F. Beirnaert, G. Dálya, and A. Ghosh, *Mon. Not. R. Astron. Soc.* **542**, 3346–3353 (2025).
 - [17] S. Mukherjee, *Mon. Not. R. Astron. Soc.* **515**, 5495–5505 (2022).
 - [18] H. Yu, B. Seymour, Y. Wang, and Y. Chen, *Astrophys. J.* **941**, 174 (2022), arXiv:2206.09984 [astro-ph.CO].
 - [19] S. R. Taylor, J. R. Gair, and I. Mandel, *Phys. Rev. D* **85**, 023535 (2012).
 - [20] S. M. Gaebel, J. Veitch, T. Dent, and W. M. Farr, *Mon. Not. R. Astron. Soc.* **484**, 4008 (2019), <https://academic.oup.com/mnras/article-pdf/484/3/4008/27738367/stz225.pdf>.
 - [21] S. Vitale, D. Gerosa, W. M. Farr, and S. R. Taylor, “Inferring the properties of a population of compact binaries in presence of selection effects,” in *Handbook of Gravitational Wave Astronomy* (Springer Singapore, 2021) p. 1–60.
 - [22] R. Abbott *et al.* (LIGO Scientific Collaboration, Virgo Collaboration, and KAGRA Collaboration), *Phys. Rev. X* **13**, 011048 (2023).
 - [23] R. Gray, F. Beirnaert, C. Karathanasis, B. Revenu, C. Turski, A. Chen, T. Baker, S. Vallejo, A. E. Romano, T. Ghosh, A. Ghosh, K. Leyde, S. Mastrogiovanni, and

- S. More, *J. Cosmol. Astropart. Phys.* **2023**, 023 (2023).
- [24] A. G. Abac *et al.*, “Gwtc-4.0: Population properties of merging compact binaries,” (2025), arXiv:2508.18083 [astro-ph.HE].
- [25] H. Gabbard, C. Messenger, I. S. Heng, F. Tonolini, and R. Murray-Smith, *Nat. Phys.* **18**, 112–117 (2021).
- [26] M. Dax, S. R. Green, J. Gair, J. H. Macke, A. Buonanno, and B. Schölkopf, *Phys. Rev. Lett.* **127**, 241103 (2021).
- [27] U. Bhardwaj, J. Alvey, B. K. Miller, S. Nissanke, and C. Weniger, *Phys. Rev. D* **108**, 042004 (2023).
- [28] D. Chatterjee, E. Marx, W. Benoit, R. Kumar, M. Desai, E. Govorkova, A. Gunny, E. Moreno, R. Omer, R. Raikman, M. Saleem, S. Aggarwal, M. W. Coughlin, P. Harris, and E. Katsavounidis, “Rapid likelihood free inference of compact binary coalescences using accelerated hardware,” (2024), arXiv:2407.19048 [gr-qc].
- [29] E. Marx, W. Benoit, A. Gunny, R. Omer, D. Chatterjee, R. C. Venterea, L. Wills, M. Saleem, E. Moreno, R. Raikman, E. Govorkova, D. Rankin, M. W. Coughlin, P. Harris, and E. Katsavounidis, “A machine-learning pipeline for real-time detection of gravitational waves from compact binary coalescences,” (2025), arXiv:2403.18661 [gr-qc].
- [30] W. M. Farr, J. R. Gair, I. Mandel, and C. Cutler, *Phys. Rev. D* **91** (2015), 10.1103/physrevd.91.023005.
- [31] S. Galadage, C. Talbot, and E. Thrane, *Phys. Rev. D* **102**, 083026 (2020).
- [32] J. Roulet, T. Venumadhav, B. Zackay, L. Dai, and M. Zaldarriaga, *Phys. Rev. D* **102**, 123022 (2020).
- [33] J. Heinzl, C. Talbot, G. Ashton, and S. Vitale, *Mon. Not. R. Astron. Soc.* **523**, 5972–5984 (2023).
- [34] A. K. Mehta, D. Wadekar, I. Anantpurkar, J. Roulet, T. Venumadhav, T. Islam, J. Mushkin, B. Zackay, and M. Zaldarriaga, “Binary black hole population inference combining confident and marginal events from the **IAS-HM** search pipeline,” (2025), arXiv:2508.15350 [gr-qc].
- [35] C. Messick *et al.*, *Phys. Rev. D* **95** (2017), 10.1103/physrevd.95.042001.
- [36] K. Cannon, C. Hanna, and D. Keppel, *Phys. Rev. D* **88**, 024025 (2013).
- [37] F. Guglielmetti, R. Fischer, and V. Dose, *Mon. Not. R. Astron. Soc.* **396**, 165–190 (2009).
- [38] B. P. Abbott *et al.* (LIGO Scientific Collaboration and Virgo Collaboration), *Phys. Rev. X* **6**, 041015 (2016).
- [39] B. P. Abbott *et al.*, *Astrophys. J. Lett.* **833**, L1 (2016).
- [40] R. Lynch, M. Coughlin, S. Vitale, C. W. Stubbs, and E. Katsavounidis, *Astrophys. J. Lett.* **861**, L24 (2018).
- [41] S. J. Kapadia, S. Caudill, J. D. E. Creighton, W. M. Farr, G. Mendell, A. Weinstein, K. Cannon, H. Fong, P. Godwin, R. K. L. Lo, R. Magee, D. Meacher, C. Messick, S. R. Mohite, D. Mukherjee, and S. Sachdev, *Class. Quantum Gravity* **37**, 045007 (2020).
- [42] A. Ray *et al.*, “When to point your telescopes: Gravitational wave trigger classification for real-time multi-messenger followup observations,” (2023), arXiv:2306.07190 [gr-qc].
- [43] I. Mandel, W. M. Farr, and J. R. Gair, *Mon. Not. R. Astron. Soc.* **486**, 1086–1093 (2019).
- [44] R. Essick, M. W. Coughlin, M. Zevin, D. Chatterjee, T. A. Clarke, S. Colloms, U. Mali, S. Miller, N. Steinle, P. Baral, A. C. Baylor, G. C. Davies, T. Dent, P. Joshi, P. Kumar, C. Messick, T. Mishra, A. Ouzriat, K. S. Phukon, L. Piccari, M. Pillas, M. Trevor, T. A. Callister, and M. Fishbach, “Compact binary coalescence sensitivity estimates with injection campaigns during the ligo-virgo-kagra collaborations’ fourth observing run,” (2025), arXiv:2508.10638 [gr-qc].
- [45] K. Cannon, C. Hanna, and J. Peoples, “Likelihood-ratio ranking statistic for compact binary coalescence candidates with rate estimation,” (2015), arXiv:1504.04632 [astro-ph.IM].
- [46] L. Tsukada *et al.*, *Phys. Rev. D* **108**, 043004 (2023).
- [47] “GstLAL,” <https://git.ligo.org/lscsoft/gstlal>, accessed: 2025-09-11.
- [48] B. P. Abbott *et al.* (LIGO Scientific Collaboration and Virgo Collaboration), *Phys. Rev. Lett.* **116**, 061102 (2016).
- [49] B. Ewing, R. Huxford, D. Singh, L. Tsukada, C. Hanna, Y.-J. Huang, P. Joshi, A. K. Y. Li, R. Magee, C. Messick, A. Pace, A. Ray, S. Sachdev, S. Sakon, R. Tapia, S. Adhicary, P. Baral, A. Baylor, K. Cannon, S. Caudill, S. S. Chaudhary, M. W. Coughlin, B. Cousins, J. D. E. Creighton, R. Essick, H. Fong, R. N. George, P. Godwin, R. Harada, J. Kennington, S. Kuwahara, D. Meacher, S. Morisaki, D. Mukherjee, W. Niu, C. Posnansky, A. Toivonen, T. Tsutsui, K. Ueno, A. Viets, L. Wade, M. Wade, and G. Waratkar, *Phys. Rev. D* **109**, 042008 (2024).
- [50] H. K. Y. Fong, *From simulations to signals: Analyzing gravitational waves from compact binary coalescences*, Ph.D. thesis, University of Toronto (2018).
- [51] J. D. E. Creighton and W. G. Anderson, “Gravitational-wave data analysis,” in *Gravitational-Wave Physics and Astronomy* (John Wiley & Sons, Ltd, 2011).
- [52] P. B. Patnaik, *Biometrika* **36**, 202 (1949).
- [53] H. Fong *et al.*, “GW070605: An Undisclosed Binary Neutron Star Hardware Injection in LIGO’s Fifth Science Run,” In preparation.
- [54] B. P. Abbott *et al.*, “Exploring the Sensitivity of Next Generation Gravitational Wave Detectors,” <https://dcc.ligo.org/LIGO-P1600143/public> (2016).
- [55] L. Barsotti, S. Gras, M. Evans, and P. Fritschel, “Updated Advanced LIGO sensitivity design curve,” <https://dcc.ligo.org/LIGO-T1800044/public> (2018).
- [56] P. Virtanen *et al.*, *Nat. Methods* **17**, 261–272 (2020).
- [57] W. M. Farr, M. Fishbach, J. Ye, and D. E. Holz, *Astrophys. J. Lett.* **883**, L42 (2019).
- [58] M. Mapelli, *Front. Astron. Space Sci.* **7** (2020), 10.3389/fspas.2020.00038.
- [59] J. M. Ezquiaga and D. E. Holz, *Phys. Rev. Lett.* **129**, 061102 (2022).
- [60] U. Mali and R. Essick, “Striking a chord with spectral sirens: multiple features in the compact binary population correlate with h_0 ,” (2024), arXiv:2410.07416 [astro-ph.HE].
- [61] LIGO Scientific Collaboration, “LIGO Algorithm Library - LALSuite,” free software (GPL) (2018).